THE UNIVERSITY OF CHICAGO

INCLUSIVE HADRON PRODUCTION IN INELASTIC MUON-PROTON SCATTERING AT 150 GeV

A DISSERTATION SUBMITTED TO
THE FACULTY OF THE DIVISION OF THE PHYSICAL SCIENCES
IN CANDIDACY FOR THE DEGREE OF
DOCTOR OF PHILOSOPHY

DEPARTMENT OF PHYSICS

BY

HOWARD S. MATIS

CHICAGO, ILLINOIS
MARCH 1976

ACKNOWLEDGMENTS

This experiment was performed by a collaboration from the University of Chicago, Harvard University, the University of Illinois, and Oxford University. Technical support was provided by the sponsoring institutions. Fermilab provided the accelerator facilities and support for the experiment. Throughout the experiment, the Neutrino Laboratory crew and the Computational Center presonnel were most helpful. At Chicago the work of T. Nunamaker and his staff of the Electronics shop was noteworthy. R. L. Armstrong and R. Byrnes, heads respectively of the Engineering Services and the Central Shop, also made substantial contributions.

All of the members of the collaboration played a part in the execution of the experiment on which this dissertation is based. I thank them for their help and for the opportunity to work in an exciting area of physics. W. A. Loomis worked closely with me on the hadron analysis. The analyses on the scaled and tertiary tapes were done by T. W. Quirk and S. H. Pordes. Conversations with W. R. Francis, L. C. Myrianthopoulos and A. Skuja provided many useful ideas.

Professor H. L. Anderson provided me with encouragement and Professor S. C. Wright, my research advisor, has given me excellent guidance and support throughout my graduate studies.

This work was supported by the National Science Foundation. The NSF provided me with a research assistantship during my studies at the University of Chicago.

TABLE OF CONTENTS

LIST OF TABLES

LIST OF ILLUSTRATIONS

CHAPTER I

LEPTON-HADRON SCATTERING

Throughout modern physics scattering experiments have been the prime source of knowledge about the structure of matter. Foremost among these are Rutherford's investigation of alpha particle scattering which led him to postulate the nuclear atom. The results of this classic experiment exhibit scale invariance--that is the cross section involves no fundamental scale of length. This feature is not surprising at low energies where the interaction, a pure coulomb type, involves no length scale. The Rutherford formula for scattering of alpha particles of mass m by a nucleus of charge Z,

$$\frac{d\sigma}{d\Omega} = \frac{(4)4z^2\alpha^2m^2}{q^4}$$

depends only on q^2, the 4-momentum transfer squared. In modern language the form factor has the value 1. This behavior persists until the momentum transfer is high enough to reveal a charge structure in the nucleus and necessitate the introduction of a length for its description. It is a surprising and remarkable result that in the highly inelastic scattering of energetic electrons by nucleons, scale invariance reasserts itself. This dissertation reports characteristics of the final state hadrons in this interesting regime. The data came from an experiment[1] with 150 GeV muons carried out at the Fermi National Accelerator Laboratory (Fermilab).

Form Factors

Before the results of the deep-inelastic muon scattering experiment will be discussed, a brief presentation of the properties of electrons and muons as probes of matter will be given. Quantum Electrodynamics (QED) accurately predicts the electromagnetic interaction among charged leptons.[2] Very accurate measurements of a variety of phenomena such as the anomalous magnetic moment of electrons and muons, hyperfine splitting of muonium, and the Lamb shift, all agree with the latest calculations of QED. Furthermore, for scattering experiments, it is sufficient to consider only single photon exchange. This is seen most clearly in the interference between the one-photon amplitude (A) and the real part of the two-photon amplitude (Re B). This interference term changes sign when a charged lepton is replaced by its corresponding anti-particle. The ratio[3] of particle to anti-particle cross section can be approximately written as 1 + 4 (Re B)/A. Any deviation from 1 shows the contribution of the two-photon process. Experiments with e^+ and e^- and μ^+ and μ^- have shown that the effect of this two-photon exchange is less than a few percent.[4]

The one-photon Feynman diagram of the interaction of a electron or muon with a proton is shown in Figure 1. The calculation of the vertex between the lepton and the virtual photon is a standard procedure in QED.[5] The unknown is the vertex between the proton and virtual photon. Cross section measurements of scattered leptons provide information on this proton-photon vertex. Rosenbluth, assuming a one-photon exchange, derived an expression for the elastic cross section. His formula generalized to the case of inelastic scattering of leptons by nucleons is

$$\frac{d^2\sigma}{d\nu dq^2} = \frac{4\pi\alpha^2}{q^4}\,\frac{(E-\nu)}{E}\cos^2(\theta/2)\left[W_2(q^2,\nu) + 2W_1(q^2,\nu)\tan^2(\theta/2)\right].$$

θ is the lab scattering angle for the lepton of total incident energy E, ν is the energy lost by the lepton, and q^2 is the four-momentum squared for the virtual photon. W_1 and W_2 are form factors or structure functions for the nucleon. They depend on only ν and q^2. These functions reflect the unknown interaction between the virtual photon and the nucleon and can be measured by inelastic lepton nucleon scattering experiments. In contrast, hadron-hadron scattering can in no way be interpreted with the same simplicity as lepton-hadron scattering. Hadrons interact with nucleons by exchanging particles. The dynamics of the interaction and even the identification of all the possible exchanges are not well known.

The SLAC Experiment

Since lepton scattering provides an excellent probe of the structure of nucleons, experimenters at the Stanford Linear Accelerator Lab (SLAC) undertook a comprehensive study of inelastic scattering of electrons by protons and deuterons.[6] A series of measurements of W_1 and W_2 were made with electrons in the energy range 4.5 to 20 GeV. It was discovered that in the region $q^2 > 1$ GeV^2 and $\sqrt{s} > 2.0$ GeV (energy of the electron-proton center of mass system), the structure functions for both proton and neutron could be parametrized by a single variable $\omega = 2M\nu/q^2$. Remarkably scale invariance had reappeared.

The Parton Model

Prior to the SLAC experiment, Bjorken[7] proposed that W_1 and νW_2 would scale for large ν and q^2. Further work by Feynman[8] and Bjorken and Paschos[9] showed that the arguments for scaling could be made more physical by the hypothesis that there are point-like constituents of hadrons, partons, which make up the substructure of matter. Partons have fixed masses and quantum numbers. Two or more bound together form a hadron and it is their interactions that are responsible for the forces between hadrons. Since partons are point particles, collisions between them can be treated more simply than between hadrons.

In real or virtual photon interactions with a nucleon, it is presumed that the photon interacts only with a single parton and except for this struck parton the rest of the nucleon is undisturbed. This is diagrammed in Figure 2. The virtual photon knocks one parton from the nucleon and then that parton and the remainder of the nucleon radiate into hadrons.

Based on these ideas the concept of scaling can be derived. The following argument[9] is illustrative. When the nucleon with 4-momentum $\underline{P}^{\mu}$ is viewed in the infinite-momentum frame, the momentum P is much greater than the mass and the partons have relatively small transverse momenta. The virtual photon scatters instantaneously, elastically, and incoherently from the point-like partons. For the i^{th} parton whose longitudinal momentum is a fraction z_i of the total nucleon's momentum, it is a good approximation to write the 4-momentum as $z_i\underline{P}^{\mu}$. In fact this is the advantage of choosing the infinite-momentum frame. The contribution of this parton with charge Q_i to W_2 is

$$W_2{}^{(i)} = z_i Q_i^2 M\delta\left[\underline{q}\cdot z_i\underline{p} - \frac{q^2}{2}\right] = Q_i^2 M\delta\left[\underline{q}\cdot\underline{p} - \frac{q^2}{2z_i}\right]$$

$$= Q_i^2\delta\left[\nu - \frac{q^2}{2Mz_i}\right]$$

which reduces to the Rutherford formula in the high energy limit,

$$\lim_{E\to\infty} \frac{d\sigma^{(i)}}{dq^2} = Q_i^2\left[\frac{4\pi\alpha^2}{q^4}\right].$$

To express the cross section in terms of all the partons in the nucleon, we need P(N), the probability that N partons make up the nucleon, $\langle\Sigma_i Q_i^2\rangle_N$, the average value of $\Sigma_i Q_i^2$, and $f_N(z)$, the z distribution in the configuration. Using these definitions we have

$$W_2(\nu,q^2) = \sum_N P(N) < \sum_i Q_i^2 >_N \int_0^1 dz f_N(z)\,\delta\left[\nu - \frac{q^2}{2Mz}\right].$$

Evaluating the integral,

$$\nu W_2(\nu,q^2) = \sum_N P(N) \langle\sum_i Q_i^2\rangle_N \; z f_N(z)$$

where

$$z = q^2/2M\nu = 1/\omega.$$

νW_2 is only a function of a single variable--that is--it scales.

Hadron Distribution Functions

Before discussing the parton model's predictions for the final state hadrons in muon-nucleon scattering, we will define distribution functions by which we describe the experimental results. The focus of this dissertation is the inclusive hadron cross sections in muon-proton scattering. That is the distributions of a single hadron in the final state are studied with no attention given to the remaining hadrons. Accordingly we are interested in the $\gamma^* + p \to h + x$ part of Figure 1. The virtual photon, γ^*, with 4-momentum $\underline{q}$ fixes the axis of the interaction. In the lab frame $\underline{q} = (E-E', \vec{p}-\vec{p}')$ and $q^2 \approx 4EE' \sin^2\theta/2$ where θ is the muon scattering angle. The "mass" squared of the final state is

$$s = M^2 + 2M\nu - q^2.$$

Hereafter, hadrons are always referred to the center of mass frame of the virtual photon and proton. P_L^* and P_T are the momentum parallel and perpendicular to the virtual photon's direction respectively and E^* is the hadron's energy. P_{max}^* is the maximum momentum that a pion can have. As s approaches infinity $P_{max}^* \approx \sqrt{s}/2$. We use the Feynman scaling variable

$$x' = P_L^* / (P_{max}^{*2} - P_T^2)^{1/2}.$$

x' can vary from -1 to +1. Another longitudinal variable is rapidity:

$$y = 1/2 \ln (E^* + P_L^*)/(E^* - P_L^*).$$

The maximum rapidity of a reaction increases with s. To facilitate comparisons of data of different s, it is convenient to eliminate this kinematic effect and define $y^* = y_{max} - y$. y_{max} is the rapidity of a pion with momentum

p^*_{max} along the virtual photon's direction. y^* is similar to y_{lab} used by ISR experimenters.[10]

As shown by L. Hand,[11] it is convenient to express the cross section for

$$\mu^+ + p \to \mu^+ + h + x \tag{1}$$

in terms of the virtual photon reaction

$$\gamma^* + p \to h + x. \tag{2}$$

The total cross section for (2) can be written

$$\sigma(q^2,s) = \frac{1}{\Gamma(q^2,s)} \frac{d\sigma}{dq^2 ds}, \tag{3}$$

where Γ is the flux of virtual photons and $d\sigma/dq^2ds$ is the differential cross section for (1). The differential cross section for (2) can be written as[12]

$$\frac{d\sigma(q^2,s)}{dp^3} = \frac{1}{\Gamma(q^2,s)} \frac{d\sigma}{dp^3 dq^2 ds}. \tag{4}$$

The relative cross section for virtual photoproduction

$$\frac{1}{\sigma(q^2,s)} \frac{d\sigma(q^2,s)}{dp^3} \tag{5}$$

is expressed entirely in terms of the relative muon cross section by dividing (4) by (3). This quantity can be conveniently measured. In this experiment, its variation with x', y^* and P_T was investigated. The variation with x' is best expressed in terms of the invariant structure function

$$F(x',q^2,s) = \frac{1}{\sigma(q^2,s)}\,\frac{1}{\pi}\int_0^\infty dP_T^2\,\frac{E^*}{\sqrt{P_L^{*2}-P_T^2}}\,\frac{d\sigma(q^2,s)}{dP_T^2\,dx'}\ ,$$

while the transverse momentum distribution is best described by

$$G(P_T^2) = g(P_T^2,q^2,s,x_1',\ x_2') = \frac{1}{\sigma(q^2,s)}\,\frac{1}{\pi}\int_{x_1'}^{x_2'} dx'\,\frac{d\sigma(q^2,s)}{dP_T^2\,dx'}\ .$$

In these formulae the derivatives on the R.H.S. are found by averaging (5) over azimuth--namely

$$\left\langle \frac{1}{\sigma(q^2,s)}\,E\,\frac{d\sigma(q^2,s)}{dP^3} \right\rangle_{\text{azimuth}} = \frac{1}{\sigma(q^2,s)}\,\frac{E^*}{\sqrt{P^{*\,2}_{\text{max}}-P_T^2}}\,\frac{1}{\pi}\,\frac{d\sigma(q^2,s)}{dx'\,dP_T^2}$$

$$= \frac{1}{\sigma(q^2,s)}\,\frac{1}{\pi}\,\frac{d\sigma(q^2,s)}{dy\,dP_T^2}$$

Theoretical Predictions

Parton models, the vector dominance model, and the thermodynamic model, all have something to say about the final state hadrons in lepton-proton scattering. A short discussion of the predictions of these theories on charge ratios, hadronic scaling, rapidity, and P_T variation follows.

Charge Ratio

The charge ratio is defined as the ratio of the number of positive to negative hadrons. Parton models have specific predictions for this ratio. As shown in Figure 2, a parton which is kicked away from the rest of the proton in the forward direction ($x' > 0$) will fragment into other particles. Those particles are bound by charge conservation and their net charge will be that of the parton which formed them. The rest of the proton will fragment. Most of those fragments are found in the backward direction ($x' < 0$) or with small x'.

A naive quark-parton model[13] assumes that the proton is made from 3 quarks which have the usual quantum numbers. Two are u-type with charge +2/3; the other is a d-type with charge -1/3. A stuck parton is assumed to radiate a hadron in the far forward direction whose charge has the same sign as the parton. Since the cross section is proportional to the square of the charge, the charge ratio is predicted to be 8.

Other parton models dilute this ratio. Dakin and Feldman[14] assume that the proton consists of a sea of u, d, and s quarks and the valence quarks. Obviously, the quarks in the sea must have null net quantum numbers. The neutral sea decreases the ratio of positive partons to negative partons and must reduce the charge ratio below 8. Dakin and Feldman have used the distributions of u(ω), d(ω), and s(ω) from the SLAC single arm experiment and some hadron data from leptoproduction to predict the variation of the charge distribution.

According to vector dominance,[15] a virtual photon changes into a virtual vector meson (ρ, ω, ϕ, and possibly ψ) diffractively scatters from the proton, and then fragments into particles. This process is possible because a vector meson has the same spin, parity and charge as a photon. The products of the vector meson will tend to go in the forward direction; the products of the proton backward. Since a vector meson is neutral, the forward charge ratio should be 1.

Hadronic Scaling

Using the basic concepts of parton theory, Feynman[16] predicted that $F(q^2,s,x')$ should scale in x' as s approaches infinity. This hadronic scaling was later derived[17] from the parton model by Drell and Yan who used a field theory approach with a transverse momentum cutoff.

Rapidity

Rapidity has the remarkable property that its difference for any two particles is the same in any Lorentz frame. Partons are assumed to interact only if their rapidity difference is less than 2.[18] Figure 3 (a) shows the assumed parton distribution in rapidity for a proton. The distribution is flat in the center and goes to zero at the edges. When a virtual photon interacts with the proton, as in Figure 2, one parton is knocked away from the others. As a result of this interaction, the struck parton has its rapidity increased, while the rest of the proton will have the original distribution except for the missing parton. This is shown in Figure 3 (b). After the collision, the partons fragment into hadrons. Because only partons with small rapidity difference interact, the distribution which is shown in Figure 3 (b) becomes smeared and then appears like the one drawn in Figure 3 (c). The parton model predicts that the hadron rapidity distribution should resemble that of the partons.

P_T Distributions.

According to various authors[19] the "size" of virtual photons is $\sim 1/\sqrt{q^2}$. As the photon becomes more massive its lifetime becomes shorter. It is expected that the average transverse momentum of hadrons increases as the photon shrinks--i.e., as q^2 increases. It is only with virtual photons that q^2 can be varied.

$\langle P_T \rangle$

The thermodynamic model[20] of Hagedorm *et al.* is one of many models which predict the behavior of the average transverse momentum. According to this model, when the virtual photon collides with a nucleon, it produces a "fireball" or "fireballs." A fireball may be thought of as a "liquid drop at the boiling point" with various particles "evaporating" from it. As the energy ($\sqrt{s}$) is increased, the temperature of the drop rises very slowly to a limiting temperature. Most of the energy goes into producing more particles, rather than raising the temperature. This model predicts that the relation for the average transverse momentum as a function of temperature (τ) should be

$$<P_T(M,\tau)> = \left[\frac{\pi M\tau}{2}\right]^{1/2} \frac{K_{5/2}(M/\tau)}{K_2(M/\tau)}$$

M is the mass of the particle; $K_{5/2}$ and K_2 are modified Bessel functions. This equation gives only a weak temperature dependence. Experiments with colliding proton beams have shown the temperature of the fireball which produces pions is about 120 MeV at $s = 25$ GeV^2 and about 135 MeV at $s = 2500$ GeV^2. In this very large s range, the temperature or average transverse momentum only increases a small amount. Measurements of the s dependence for $<P_T>$ from virtual photon interactions should show the same weak behavior.

CHAPTER II

THE EXPERIMENT

The apparatus used in this study of the reaction

$$\mu^+ + p \rightarrow \mu^+ + \text{hadrons}$$

is shown schematically in Figure 4. This spectrometer was designed to measure the vector momentum of incident and scattered muons as well as the forward going charged hadrons. The horizontal direction before and after the dipoles (1E4) and the vertical direction of each incident muon was determined by 4 small multi-wire proportional chambers (MWPC's) which are labeled S0. These measurements determined the momentum and position of muons entering the target (LH). If a muon interacted in the target, the products of that reaction were detected by another set of MWPC's labeled S1. Particles scattered in the forward direction were bent by the field of a large aperture magnet CCM. This magnet was previously part of the 450 MeV Chicago Cyclotron. Sets of spark chambers, S2, S3, and S4 measured the trajectories of the particles after they were bent by the CCM. The tracks found in chambers S1-4 provided the information needed to calculate the vector momentum of products of the muon interaction. A very large chunk of steel (A) absorbed the hadrons produced in this interaction. Only muons could penetrate this shield. Muons were detected by spark chambers S4. Matching the track found in S4 with the tracks found in S1-S3 identified the scattered muon. The fast electronics, using counters B, V, G, N, M, and M', signaled an "event" when a muon in the beam scattered through some angle and/or lost some energy. Upon the occurrence of an event, triggering was suspended, "live-time" scalers were halted, all discriminators and set wires in the proportional chambers were latched and the spark chambers were triggered. Some 20 μsec later when all spark noise had died down, counter logic, scaler information, addresses of sparks and set wires were retrieved and recorded on tape by a Xerox Σ-3 computer. Finally, the apparatus was reset and armed for the next event.

Muon Beam

A 300 GeV proton beam, produced at Fermilab, was used to produce muons. Figure 5 shows a schematic of the muon beam line. 300 GeV protons hit a foot long aluminum target (TO) and radiated hadrons. Magnets Q0 focused the charged products into a 2400' drift space. π's and K's decayed into muons which, because of their high energy, traveled along the beam direction. Dipoles D1-3 guided the particles to the muon laboratory. Quadrupoles Q1 focussed the beam onto 63' of CH_2, a length sufficient to absorb the hadrons. The final hadron to muon ratio was ($\sim 10^{-5}$). The field of quadrupoles Q2 refocussed the muons onto the hydrogen target. The last dipole, D3, was used to momentum analyze the muons.

Momentum Measurement of the Incident Muon

Eight inch square beam MWPC's and three dipole magnets with four inch diameter apertures were used to determine the momentum of the muon. Two pairs of horizontal MWPC's defined the trajectory of muons before and after the dipoles. Beam hodoscopes, which covered the active area of all chambers, were used to check that tracks were formed within 15 ns of a trigger. A simple calculation of the bending angle for the tracks upstream and downstream of the dipoles produced the muon's momentum to an accuracy of ∿0.5%. This section of the apparatus accepted muons which had a momentum of 150 GeV with a spread of about 3% FWHM. Besides the momentum of the muon, the position of the muon at the target was needed. The last two horizontal beam MWPC's together with two adjacent vertical MWPC's completed the definition of this trajectory. With the vector momentum of both the incident and scattered muon, q^2 and ν could be determined for each event.

LH_2 Target

The target was a mylar flask, a cylinder 1.2 m long 7" in diameter, filled with LH_2. It was enclosed in a thin walled evacuated aluminum cylinder which protected and insulated the flask.

Measurement of the Scattered Particles

Particles scattered forward in the target were momentum analyzed. They were detected with 4 horizontal and 4 vertical 1m square proportional chambers[21] (S1). The field of the CCM deflected the particles with a transverse kick of 2.2 GeV. Twenty wire planes measured the trajectories downstream of the CCM. The first set (S2) were the 12 2m x 4m planes with shift register read-out;[22] the second set (S3) were 8 2m x 6m planes with magnetostrictive read-out. Tracks found in these chambers were linked with tracks found in the proportional chambers. Figure 6 shows the distribution for linking error in the horizontal direction. The FWHM is 6 mm. For 100 GeV particles $\Delta P/P \approx .015$. The charge of each particle could be clearly identified. A vertical hodoscope, H, and a horizontal hodoscope, G, provided an array of counters that were used to check if a track was intime.

Muon Identification

To specify q^2 and ν, the muon had to be selected from the tracks downstream of the CCM. This sorting was done with an 8' thick block of steel which absorbed all particles but muons. Vertical and horizontal hodoscopes, M and M', plus 8 magnetostrictive 2m x 4m planes were used to detect the scattered muon.

The Trigger

The apparatus, just described, was sufficient to specify an inelastic scattering. Since only one of every million muons scattered with a proton, it was necessary to use a series of counters and fast electronics to select events. The electronic logic demanded that there be both a muon in the beam line incident on the target and a scattered muon. The trigger was defined as a coincidence of B, G, and (M or M') and an anti-coincidence of V and N. Signal widths from B and N were 15 ns, and from the V, G, M and M' arrays about 20 ns.

B represents four counters shown in Figure 4. Any muon passing through all these counters would travel through the target and therefore be considered a possible candidate for a scatter.

Three hodoscopes, G, M, and M', determined if the muon left the beam. Each hodoscope had a hole where the beam passed. If any element of a hodoscope was set, a particle was outside the beam. Since only a muon could penetrate to M and M', one element set from either was necessary for a trigger.

Another hodoscope array, N, was run in anti-coincidence. For a trigger a muon had to scatter sufficiently to avoid this array. The N, 54 cm x 66 cm, was centered on the beam and located behind the hadron absorber.

A 2m x 4m array of counters, V in Figure 4, detected halo muons, muons which were incident upon the apparatus but not the target. Because of the characteristics of the beam line, the ratio of beam to halo was about 1. Halo muons contributed to spurious triggers and made track reconstruction more difficult. To avoid problems all elements of V were put in anti-coincidence with the trigger. To exclude events with more than 1 muon in the target, triggers were restricted to no more than one element set for either the last horizontal or vertical beam hodoscope.

In summary, any trigger had to pass four conditions. Only a single beam particle was present. A G counter was set. An M or M' counter was set. No N or V counter was set.

Electronic Read-Out

The output of the counters were stored in CAMAC latches. Signals from the counters were adjusted so the pulses formed by a particle arrived at the latches at the same time. When the electronic trigger logic was satisfied, a strobe was sent to the latches to store the signals from the counters at the time of the event.

In addition, a strobe was sent to the proportional chambers to store the set wire addresses in a shift register. Shift registers also stored spark addresses in some of the spark chambers. After the spark noise from an event had died out, CAMAC scanners interrogated each shift register and stored the addresses of set wires in a small memory. For each spark, the last wire and the total number of wires up to seven that were struck were stored. ("Sparks" here are also defined as set-wires in MWPC's.) If more than seven adjacent wires were struck, the spark was broken into multiples of seven wires. Each scanner could handle 64 sparks. MWPC's contained few sparks per event so that a scanner could hold many planes without the data overflowing its buffer. One scanner was sufficient to store all the beam chamber sparks; the 1m MWPC's shared two scanners. Since spark chambers had many sparks per event, each plane was connected to a separate scanner.

The magnetostrictive spark chambers used a different readout. Pulses had to be digitized before they were stored in a scanner. First, the pulses from the magnetostrictive wands were sent to a discriminator. The time of arrival of the center of the signal was compared to a 20 mhz clock. This time was stored in a CAMAC module. Two scanners were used in this experiment and each could hold 600 sparks.

In addition to the counters and chamber data, CAMAC quad scalers stored information which was used to calculate various rates. The number of beam muons and halo muons passing through the apparatus was collected in those scalers as well as data needed to calculate random rates and deadtime.

The Online Computer

The online computer for this experiment was a Xerox Σ-3 equipped with a 64K fast memory, line printer, teletype, two 9 track tape drives, 750K disk storage, display scope, sense switches, and a branch driver interfaced to the CAMAC system. The Σ-3 has a priority interrupt structure that permits fast switching between a number of tasks with complete context storage of interrupted tasks. In order of priority the program tasks were: event acquisition, tape writing, and background processing and surveillance

The event task was entered by an interrupt, 5 ms after a trigger. All event information was read through the CAMAC interface. First the counters and scalers were read. They were stored in the first 120 words of the data buffer. Then, the computer processed the chamber information. Data was written in 600 word blocks. No more than four blocks were permitted per event. However, during the whole running period no event ever needed more than four. A typical event fitted into two. The computer processed an average event in 50 ms. When the computer finished reading the CAMAC data, it gated the experiment on and exited from the event task.

Events during a beam spill, about 1 second of muons every six seconds, were stored in the computer's memory. 20 blocks could be handled per spill. However the computer gated the experiment off whenever the maximum four records for the next event could not fit inside the buffer in order not to bias the experiment by taking short record events and rejecting long ones.

Following the beam spill the computer entered the tape task and wrote all the data onto tape in 600 word records. Typically, the computer would write 5500 events onto a single tape. When the tape was full, the run was ended and a new tape mounted. Each run had at its beginning seven records of information. This information included active chamber and counter positions, locations of CAMAC modules, comments, and some other useful information. These records provided sufficient information so that tapes could be processed "offline."

When not carrying out the tape or event task the Σ-3 conducted the background tasks of analyzing events and monitoring equipment. Through various sense switches, many displays could be requested. On the storage scope, the computer drew pictures of the equipment. Sparks and tracks were indicated. At a glance we could tell whether a chamber was off. Beam profiles were shown. Chamber efficiencies were monitored. There were complete line printer tables of rates and statistics on chambers and counters. On request, all the data from one event could be listed on the line printer. Errors in readout and for a misbehaving counter could easily be found.

There were consistency checks for the digital chamber scanners. All addresses had to be ascending. The number of successive wires struck had to be consistent with the specification of the scanner. Set wires in the 1m MWPC's and shift register spark chambers had to be found. If data did not satisfy any consistency checks, there was some improper operation in the electronics. The magnetostrictive chambers were checked in a slightly different way. Because magnetostrictive pulses traveled at the speed of sound, temperature and tension changes affected their velocity. Since these chambers were not digital, some method of calibrating the pulses along the magnetostrictive wands had to be used. Fiducials, whose positions were accurately known, were placed at the beginning and at the end of each plane. On every sampled event, fiducials were checked to be certain they did not drift more than a few counts. Missing fiducials indicated that there was something wrong in the electronics. Addresses of sparks had to be in ascending order for each plane. Again, any deviation shown in these checks indicated a malfunction.

The computer stored statistics on all those malfunctions in its memory. At the end of each run or on request, a printout of all such errors was made. In this way, troubles could be quickly spotted and corrected.

Besides monitoring the chambers, the computer made automatic checks on the CAMAC modules. At the beginning and end of every run each module would be tested. Any malfunction would be reported on the line printer. The

Σ-3 checked that data was actually sent to the modules for every event. It also made sure that the modules gave correct responses to the computer's orders. Any error in any CAMAC response caused the computer to stop looking at the event. The Σ-3 would disregard the data, write an error message on the line printer, and continue reading events. Therefore, all events recorded on tape had perfect CAMAC behavior.

CHAPTER III

DATA ANALYSIS

The data from the completed run were recorded on 67 magnetic tapes. This represents events from 2.1×10^{10} muons incident on the 8.4 g/cm^2 liquid hydrogen target. The reconstruction of events from the tape record was an extremely complicated task. The analysis was split into three parts. First, the raw data tapes were used to find the position of the chambers and counters. This was important since it turned out that the mechanical survey was off in some cases. Next, the sparks were converted into coordinates and written on another tape. Finally, a program used these "scaled" tapes to carry out a track analysis, and the kinematic description of each event was written on a tertiary tape. The physics analysis was carried out by programs using these tertiary tapes.

Scaled and tertiary tapes were produced at the Rutherford Laboratory's IBM 360/195. The physics analysis was performed at Fermilab's CDC 6600 computer.

Scaled Data Tapes

Raw data tapes were first processed into scaled tapes. Scaled tapes have the spark chamber and MWPC data referred to a standard right handed coordinate system in which positive y is in the vertical direction, positive z is along the beam direction, and the origin of the system is the center of the CCM.

The beam MWPC's had been accurately positioned in a mechanical survey and the alignment of the remaining chambers was referred to them. This was done by finding the displacements for each plane which minimized the χ^2 for tracks passing through that plane. This procedure was performed each run.

First the 1m MWPC's were aligned with respect to the beam chambers. x and y alignments were done separately because there was not enough information to uniquely determine which x and which y track belonged to the same particle in those chambers.

Next, the relative positions of the hadron chambers (6m and shift register) were found. In practice, only the magnetostrictive parameters changed each run, since for them the timing of signals from the fiducials drifted. The origin of this effect was that the speed of the pulses in the magnetostrictive wands changed with temperature fluctuations. Some wands had a non-linear behavior and appropriate corrections were made for these.

Following this, the hadron planes were aligned with respect to the proportional chambers by linking tracks through the CCM. To link tracks it is necessary to know the effect of the CCM on a particle. The magnet's cylindrically symmetric field bends particles in the horizontal plane. Because of the symmetry of the field, the impact parameter is the same on entry and exit. Because most entry trajectories were nearly radial, vertical focussing was negligible. Tracks entering and exiting the CCM were linked by matching impact parameters and y trajectories. That displacement of the hadron chambers, which did this best, determined the alignment.

The last task was to align the muon chambers. These planes were aligned among themselves first. Then, the muon module was aligned with respect to the hadron chambers again using tracks.

Once the alignment was complete, the computer rewound the tape. The data was transformed into the canonical coordinate system and this information was written on a scaled tape.

Tertiary Tapes

The computer first attempted to identify the incident muon. Dubious events were not used. Events, which had two muons in the beam chambers within the resolving time of the apparatus were rejected. In addition, there had to be sufficient information to unambiguously identify a beam muon. If a beam plane had only one spark, that spark was selected. If there were two or more sparks, that spark which was covered by a set beam hodoscope was selected. If there were no sparks, then the center of a uniquely struck hodoscope was taken. One of these criteria had to be satisfied for each of the first 4 beam planes. Sparks had to be found for the last two planes. Those sparks were needed to accurately point to the vertex of the event. Horizontal tracks, before and after the muon tagging magnets, were required to meet within a few millimeters at the center of muon tagging magnets. If a beam track was not found, the computer did not process the rest of the event. Typically 65% of all triggers passed this initial test.

Next, the 1m MWPC's were searched for tracks after the target. All 3 and 4 spark tracks were found. Every track had to either cross the muon in the target or point upstream to the muon. For tracks sharing two or more sparks, the track with the best χ^2 was kept.

The trackfinder then operated on the muon chambers. Adjacent planes had wires which were rotated with respect to each other. Sparks, from the planes of each gap, were turned into x and y coordinates. The trackfinder first chose an x spark from one of the 4 gaps in the muon module. It then searched the other gaps for at least two sparks which formed a roughly straight line and did a χ^2 calculation on those sparks. Sparks 1.25 mm or more from the line were dropped. If three or more sparks remained from that cut, the trackfinder searched appropriate y sparks. The χ^2 was redone. Because the y resolution was poorer than the x, the computer accepted the y sparks within 12 mm of the best line. Sparks that did not meet these criteria were dropped. If there were three of four satisfactory sparks, the computer stored the track and removed those sparks from the list. The trackfinder then continued its procedure until all possibilities were tried.

After finding all the tracks in the muon chambers, the trackfinder turned to the hadron chambers. First, tracks were found in the magnetostrictive chambers because these had fewer extraneous sparks than the shift register chambers. The method was identical to the one used on the muon chambers. The tracks that were found were then projected through the shift register planes. For y, a line was drawn from the target to the y position at the 6m chambers. Any spark within 25 mm of this line was accepted. If there were 6 sparks found, a χ^2 was calculated. The trackfinder removed any spark more than 1.75 mm away from the best line. Whenever there were no sparks found, the computer would move the initial line 15 mm at the most upstream plane and then refit the planes. 95% of the tracks were fit with the shift register chambers.

Next, tracks were linked upstream and downstream from the magnet. Since x and y tracks were not correlated in the 1m chambers, linking had to be done separately for each coordinate. Impact parameters were compared for x tracks. All tracks which matched within 8.75 mm were linked. Any pair of y tracks which satisfied the equation,

$$(\text{Slope difference}/6\ \text{mr})^2 + (\text{intercept difference at } z = 0\ /2\text{cm})^2 < 1,$$

were declared linked. The computer stored all the links for each track up to a maximum of 4.

Muon and hadron tracks were checked to see if they were "intime." Intime meant that a set element in the G or H hodoscope intercepted the track. The dimensions of the counters were expanded by 1 cm in x and 3.81 cm in y to allow for uncertainties in the survey and the tracks.

Tracks were linked between the hadron and the muon chambers. At the center of the hadron absorber, the difference in y of the two tracks had to be less than 18 cm and the x difference had to be less than 3.5 cm. The difference of the x slope had to be less than 15 mr. When there were more than one linking track, the best x link was chosen. Particles with low energy had the x criteria slightly relaxed.

Finally, intime muons were chosen. Muons were classified according to the number of counters, G, H, M, and M', that were hit. Muons had to hit a G or H and an M or M'. The more counters that a track hit, the better "quality" was assigned to the muon. The computer tested all hadrons tracks which did not have a muon link against the M and M' hodoscope. Tracks which pointed to a hit counter were identified as muon candidates. This method added 2% to the total list of possible muons. The muon track with the best quality was selected as the scattered muon.

To recover some tracks missed in the MWPC's, the trackfinder used hadron tracks. Any hadron track which did not link in x or y to a MWPC track was used as a starting point. The program searched the 1m MWPC's for two other sparks which formed a straight line with the interception of the downstream track at $z = 0$. Tracks, which were found in this manner, were included in the total list of 1m tracks.

Using all the 1m tracks and the incident muon track, the computer calculated the best vertex for the event. Following this, momenta of all linked hadron chamber tracks were computed. The trackfinder only used the vertex and the hadron chamber tracks. It used a hard-edge field model. This model is accurate to 0.07%. Tracks which were bent to positive x were declared negatively charged. Tracks which were bent to negative x were declared positive. Finally, values for q^2 and ν were obtained. After finishing these calculations, the computer wrote all the tracks and the kinematic information for each event on a tertiary tape.

The trackfinder was carefully tested. Checks were made for inefficiency and spurious events. To check for efficiencies, a random track was inserted in an event on a scaled data tape. The trackfinder tried to find that track.

According to this test, the trackfinder found 96.5% of all tracks, and no spurious tracks. However, the efficiency for finding tracks in a band between x = -50 cm and x = 20 cm was only 81%. In this region, there were many tracks left by the halo and this made trackfinding difficult. The efficiency of the trackfinder was included in the physics analysis.

Hadron Analysis

Because of the length of the spectrometer, only stable hadrons such as π's, K's and p's could be detected. Previous experiments have shown that pions are the dominant product of lepton-hadron interactions. Since the apparatus had no features that could be used to identify a particular hadron, all particles which were not classified as muons were assumed to be pions. Tracks which were listed on the tertiary tape were analyzed to determine if they were hadrons produced in an inelastic event.

First, tracks downstream of the CCM were examined. All hadrons had to be intime. Each hadron must have hit either a G or H hodoscope element. In the areas where the G and H overlapped, only one hodoscope hit was required. In that region, the quality of tracks which hit both hodoscopes and those which hit only one could not be distinguished. All hadron tracks must have been associated with at least one shift register spark chamber. This was necessary for good y resolution since the 6m chambers were very close together and consequently their resolution in y was poor. In the y dimension tracks had to point within 6 cm of the event vertex. This cut insured that all particles passed through the target.

Next, to be accepted, a downstream hadron track had to link to a track before the CCM in x or y. That information was on the tertiary tapes. In addition, the MWPC track had to be within 7.5 mm of the vertex divided by a factor. The factor, $(1.0 + m_h^2/\theta_\mu^2)^{1/2}$, where θ_μ is the scatter angle of the muon and m_h is the slope of the hadron track, accounted for the fact that the smaller the scatter angle of the muon, the harder it is to fix the vertex.

A track in the hadron chambers, which might be due to a halo muon was tested a little more carefully. Such tracks had to link both in x and y. Both x and y tracks had to meet the vertex criteria discussed above. Of course any hadron track that might have been a muon could have been eliminated but that stricter cut would have thrown out more positive than negative hadrons from the sample. Even though positive hadrons populated the same area in the chambers as the halo, there was no indication that the looser cut let any halo into the sample.

For a proper normalization, the hadron identification efficiency had to be determined. Two methods were used.

The cruder method was a visual scan of 200 events. Sparks and tracks were superimposed on a diagram of the apparatus for each event. Hadron tracks, found by the computer, were identified. A search was made for additional hadron tracks. The efficiency was calculated by finding the ratio of tracks found by the computer and the total tracks found. This method yielded an efficiency of 95%.

The other method defined a good track as one which passed all but one cut. The inefficiency of a cut was simply the number of good tracks which failed that cut. The results are shown in Table 1. The table indicates that the 1m MWPC's were slightly inefficient. The lack of redundancy in those chambers contributed to this lower efficiency. To increase the hadron efficiency, cuts 3 and 4 of Table 1 were logically ORed. With this the identification efficiency was 89.7%. The efficiency showed no spatial dependence. This method led to a lower efficiency than that found by the visual scan because the computer is a better trackfinder than the human eye.

Using a conservative approach, we declare that the efficiency for hadron detection is 90% ±5%. This correction was used when the physics results were calculated.

Besides, the μ-p events, the data tape had records of μ-e scatters, muon scattering from non-hydrogen nuclei, random triggers and other processes. These uninteresting events were separated from the sample by various cuts.

Kinematic cuts enabled the μ-e and elastic μ-p events to be removed. All events had to have a value of q^2

greater than 0.5 GeV^2. This cut is much larger than the maximum q^2 of 0.15 GeV^2 for μ-e events. Because the vertex resolution is poor at low q^2, 0.5 GeV^2 was chosen as sufficiently high to include resolution effects. The second kinematic cut was to remove all events with "s" less than 20 GeV^2. This cut eliminated elastic μ-p events and μ-p events in the resonance region.

A vertex cut was necessary to eliminate muons which scattered from non-hydrogen nuclei, such as the windows which protected the target. Figure 7 shows the reconstruction of the vertex. Events from LH_2, from the upstream target window, and from the last beam hodoscope can be clearly seen. Using the information from the figure, we only allow events with a vertex within 1.13 m of the target center. This cut excluded events from the beam hodoscope and the upstream window. The only non-LH_2 material, included in this cut, was the target flask ends and the downstream window. The mass within the cut was 95.4% LH_2. Data taken with an empty target verified that number.

Each event which passed the preceeding cuts was checked for energy conservation. The excess energy is defined by the sum of the energies of the hadrons and the scattered muon minus the energy of the incident muon. Figure 8 shows that only 1.5% of all surviving events have an excess energy greater than 4 GeV. Intime halo muons which pass near the vertex often caused this energy imbalance.

These extraneous particles generally have an extremely high transverse momentum because they are not associated with the scattering. Because almost all hadrons have $P_T^2 < 1.5$ GeV^2, these halo particles were eliminated by demanding that $P_T^2 <$ 2 GeV^2. In addition, any particle with energy greater than ν + 4 GeV was not allowed in the sample of events.

Hadron Acceptance

The acceptance was calculated for all hadrons which survived the cuts described in the last section. To obtain the acceptance, the momentum vector of a hadron was rotated in uniform steps around the direction of the virtual photon. At each step tracks, with the same origin, charge, and momentum as the original hadron, were projected through the apparatus. The acceptance was simply the fraction of those tracks which passed through the experimental apertures.

These apertures were the CCM and the shift register and 6m chambers. All tracks were first projected through the CCM using a hard-edge field model with vertical focusing. A fictitious plane at $z = 5.2$ m represented the shift register chambers. At that plane, to be accepted, the track had to have $|x| < 1.82$ m. That number was chosen instead of the chamber half-width, 2.0 m, to exclude possible edge inefficiencies. The size of the 6m chambers determined the last aperture. Accepted tracks had to hit within 2.50 m in x and 0.95 m in y of the center of these chambers. As with the shift register planes, these numbers were made smaller than the physical dimensions of the chambers to eliminate edge effects. These 6m chambers had a deadened area of 8.9 cm in radius centered on the beam. This circle was enlarged to a radius of 15.5 cm and accepted tracks were required to pass outside it. There were some indications that the chambers were inefficient when a radius of 13.0 cm was used. However, there was no difference between 15.5 cm and 18.0 cm radii.

Two implicit assumptions are contained in this method of computing the acceptance. The first assumption is that hadrons are produced uniformly around the virtual photon direction. Within statistics, this assumption was found to be true. The second is that events not seen can be included in the sample by the weight given events that are. This method clearly does *not* apply to any class of events of which none are seen. For each muon scattering, such a class will be defined by two longitudinal momenta, p_{min} and p_{max}. Any hadron with momentum inside these limits will have a finite acceptance. p_{min} and p_{max} are functions of the event origin and the virtual photon 4-momentum. The following method was used to calculate p_{min}. The momentum of a hadron with no transverse momentum, which would pass through the vertical edge of the 6m chambers, was found. 0.4 GeV (in the laboratory frame) was added to that limit to eliminate effects of multiple scattering and the resolution of the chambers. A similar procedure was used to calculate the high momentum cutoff, but for this case the cutoff was the 6m deadener. A hadron with the maximum allowed longitudinal momentum was projected through the CCM. If the hadron missed the deadener, then this momentum was p_{max}. Otherwise p_{max} was found by reducing this maximum value until the hadron missed the deadener and then subtracting another 0.4 GeV for safety. p_{min} and p_{max} were found for both positive and negative hadrons.

The effect of the low momentum cutoff is shown in Figure 9 (a) which shows the intercept of particles with longitudinal momentum $p_l < p_{min}$ at the 6m chambers. Each circle in that figure represents the intercepts of particles with the same p_l and various transverse momenta. Only particles whose circles intercept the active areas of the chambers can be detected. Since some circles miss the chambers entirely, there are some regions of P_T which have no acceptance at given p_l. Figure 9 (b) shows that all contours for particles, that have momentum > p_{min}, intersect the chambers and therefore all those particles have some acceptance. A similar argument can be made on the effect of the high momentum cutoff.

These limits p_{min} and p_{max} were used to calculate x'_{min}, the value of x' which corresponds to $P_L = p_{min}$ and $P_T = 0$. x'_{max} is found in an analogous manner. All values of x' within these limits have a finite acceptance.

Those events for which the projection of the virtual photon landed above or below the boundaries of the 6m chambers also had regions of no acceptance. Figure 9 (c) shows the intercepts of particles at the 6m chambers for events of this type. It is seen that such particles much have a minimum P_T before they can be detected. All events which belonged to this class were removed from the data sample.

The Distribution Functions

After all the cuts were applied and the hadron acceptance found, the physics results were calculated. The data were divided into regions of x', charge, q^2, and s. Because the bins of q^2 and s were large, it was necessary to examine the variation of the muon acceptance over the bins. Figure 10 shows the calculated muon acceptance. The acceptance is very high and uniform for the detected events, except in the region $q^2 < 2.0$ and $\nu < 100$. Therefore, its variation does not significantly affect the hadron distributions. When the muon acceptance was included in the analysis, this was confirmed.

Figure 11 presents a $q^2 - \nu$ plot for the detected events. These were the events used to calculate F(x'), rapidity distributions, charge ratios, $G(P_T^2)$, and $<P_T>$.

F(x')--The Invariant Structure Function

F(x') was the first function to be calculated. F(x') is the number of hadrons within Δx' times the energy, per muon, restricted to events with a specific range of q^2

and s. To avoid biases the following procedure was adopted to estimate $F(x')$:

1. Events were collected according to their range of q^2, s and charge. This defined a class. Each class was divided into bins of x'.
2. For each event of a class, x'_{min} and x'_{max} were determined and a histogram for muons as well as for hadrons was accumulated.
3. For each event the muon histogram was incremented in all bins for which x' fell between x'_{min} and x'_{max}. The hadron histogram was incremented in the appropriate bin, by the reciprocal of the hadron acceptance times a kinematic factor if this bin fell between the limits.
4. The final distribution $F(x')$ was the bin to bin ratio of these two histograms.

Two factors were needed to correct $F(x')$. The first factor was used to remove from the sample those events where the muon elastically scatters and radiates a photon. Such events appear to be inelastic, but since they have no forward hadron associated with them, they bias the determination of $F(x')$. The procedure of Mo and Tsai[23] was used to estimate this number of radiative events in terms of the total events. $F(x')$ was corrected accordingly. The radiative correction was 1.0 for all bins except for the region $s > 100$, where it was 1.31 in the $0.5 < q^2 < 3$ bin and was 1.05 in the $3 < q^2 < 10$ bin.

The second factor was a rescattering correction. It was estimated that 6% of the hadrons would interact in the target. However, most secondaries produced in the hadron interaction could not pass through the CCM. Those secondaries, which were detected, had lost some of their original longitudinal momentum. They only contributed to regions of much higher statistics, so their effect was negligible. To correct for rescattering in the analysis, F(x') was increased by 6%. This correction was also included in the other physics results.

Rapidity

A similar method to the one used to calculate F(x') was needed to find the rapidity distributions. The minimum rapidity for each event was that for a particle with $P_L = p_{min}$ and $P_T = 0$. To obtain the maximum allowed rapidity, P_L was set equal to P^*_{max}, and P_T was the minimum transverse momentum for which the hadron missed the deadener.

Charge Ratio

The charge ratio was obtained by dividing the weighted number of positive hadrons in one bin by the weighted number of negative hadrons in a corresponding bin. However, because of the deadener in the 6m chambers, the acceptance was very asymmetric for high momentum negative and positive hadrons. To symmetrize the acceptance a virtual deadener was introduced. The virtual deadener was calculated by finding the position to which the virtual photon pointed at the 6m chambers and reflecting the real deadener about the vertical line through that point. Events were weighted with an acceptance that was calculated with both the real and virtual deadeners. All hadrons had to have a momentum greater than the larger of p_{min} for either positive or negative hadrons.

P_T Distributions

Hadrons were binned in P_T^2 in different regions of q^2, s, x', and charge. Each histogram of $G(P_T^2)$ was fit to exponential functions by a CERN developed program MINUIT.

$<P_T>$

The average value of P_T as a function of x' was examined.

$$<P_T> = \sum(w^i P_T^i)/\sum w^i$$

where w^i is the inverse of the acceptance for the i^{th} particle with transverse momentum P_T^i. $<P_T>$ was calculated as a function of x' for both positive and negative hadrons.

CHAPTER IV

RESULTS

Table 2 is a summary of this and other experiments on hadrons from lepto-production.[12,24-27] The kinematic boundaries and types of detectors are listed. The table shows that this experiment covers a range of q^2 and s that has never been investigated and has only a small overlap with previous measurements. The table also lists the type of lepton used in each investigation. No difference in the data has been found between electrons and muons as the source for virtual photons.

F(x')

Figure 12 presents F(x') in different q^2 and s regions for this experiment. There is very little difference among the graphs. Within statistics, Feynman hadronic scaling appears to hold. The best exponential fit to all this data is 0.34 exp(-3.4x'), the dotted lines shown in the figure. For comparison the best exponential fit to the negative hadron distribution in the s range 12 to 30 GeV^2 measured by Dakin *et al.*[12] is 0.35 exp(-3.25x'). It should be kept in mind that exponential fits are not expected to hold for x' near 0. Only a very small charge asymmetry can be seen in the present data. Dakin *et al.*[12] however, found that F(x') for positive hadrons was everywhere greater than for negative hadrons.

There is no evidence for a rise at high x'. DESY results[25] for negative pions show an enhancement near x' = 1 in the resonance region ($s \sim 1\text{-}2\ \mathrm{GeV}^2$) and at low q^2. This rise, which goes away as s or q^2 increases, can be accounted for by nucleon resonance production.

It is very interesting to compare F(x') with results from other interactions. Figure 13 gives a convenient summary of F(x') for various particles.[28] Like pion processes, such as $\pi^{\pm} + p \rightarrow \pi^{\pm} + X$ show a peak at x' = 1. However, "unlike" pion processes, $\pi^{\pm} + p \rightarrow \pi^{\mp} + X$ show the same exponential behavior as found here. The rise in F(x') for hadron data is probably caused by the hadron exhibiting the quantum numbers of the projectile at large x'. The reactions, $p + p \rightarrow \pi^{\pm} + X$, show slightly larger slopes than unlike pion scattering. It is remarkable that the intercepts at x' = 0 of the graphs in Figure 13 are close.

Rapidity

Figures 14 and 15 show the rapidity distribution for two s regions. Since no q^2 variation was found, all values of $q^2 > 0.5\ \mathrm{GeV}^2$ were included. This figure shows no apparent charge asymmetry. There is no s difference except for the fact that the high s graphs covers a larger range in y^*. The plateau predicted by the parton model is not apparent. Superimposed on the figures are rapidity distributions at $s = 376\ \mathrm{GeV}^2$ for pion-proton interactions.[29] Our results have a similar shape and have a magnitude which is approximately the average of the π^+ and π^- curves. The charge asymmetry in the pion processes is due to the charge of the incident hadron appearing in the projectile fragmentation region. The rapidity distribution for the reaction[28] $p + p \to \pi^+ + X$ has about the same shape and magnitude as the $\pi^- + p$ curves and therefore is similar to this data.

Charge Ratio

The charge ratio is presented in Figure 16. For x' less than 0.4 the ratio is 1. It is >1 in the region $0.4 < x' < 0.85$. For more definitive statements on the q^2 variation a significant improvement in the statistical accuracy of the data is necessary.

Figure 17 compares the ω dependence of the charge ratio at high x' with previous experiments. Since most of the data is above 1, a non-diffractive theory is likely to describe the data. The predicted ω behavior of one such theory, the Dakin and Feldman quark-parton model[14] is shown in the figure. The data is consistent with that theory.

P_T Distributions

$G(P_T^2)$ was fitted to the following three functions:

$$\exp(-bP_T^2) \qquad P_T^2 < .54 \qquad \text{(A)}$$

$$\exp(-bP_T) \qquad \text{(B)}$$

$$\exp[-b(P_T^2 + M^2)^{1/2}]. \qquad \text{(C)}$$

Figure 18 presents the fits to function (A), while Figure 19 shows the fits to function (B). No q^2, s, or charge difference is apparent. Since there is no variation with q^2, the shrinking photon effect is not seen at these energies. Previous lepton scattering experiments[30] have shown that equation (A) gives a good fit to the data up to $P_T^2 = 0.4$ GeV^2. In this experiment this is also the case for $P_T^2 < 0.54$ GeV^2, and the slopes agree very well with other lepton experiments. It is seen from Figure 18 that b is about 5.5 GeV^{-2} for $x' < 0.5$ and less for $x' > 0.5$.

Figure 20 presents the data for $P_T^2 < 1.5$ GeV^2 summed over q^2 to decrease the statistical errors. The figure shows a deviation from an exponential fit in P_T^2. Data from the Santa Cruz-SLAC streamer chamber experiment[26] had indicated a break around 0.3 GeV^2. Their data was limited to $P_T^2 < 0.85$ GeV^2. Function (C) was chosen to reduce to (A) at low P_T^2 and to (B) at high P_T^2. Table 3 shows the fits for all three functions. Clearly, (C) gives the best χ^2 per degree of freedom. A display of the b, M fits in various x', s regions is shown in Figure 21. Most of the points cluster around a slope of 6. It is remarkable that the slope is the same as that found in pion and proton interactions by experiments at the ISR and Fermilab in this P_T range.[10,31] The high x' points cluster about a value of 1 GeV for M.

$<P_T>$

To determine the x' behavior of the transverse momentum, $<P_T>$ was calculated. Figure 22 shows the behavior of it as a function of x'. There appears to be no charge difference or s dependence. The "fireball" model predicts that as s increases, the excess energy in collision produces more particles and only slowly increases the average transverse momentum. The statistics are insufficient to see any such dependence in the data. However, the data rule out any strong s variation.

$<P_T>$ from hadron experiments are characterized by the "seagull" effect, a rise and then a fall in the average transverse momentum with x'.[32] The data of this experiment show that the $<P_T>$ first rises linearly with x' and then flattens. Better statistics are needed to determine whether the seagull dip is present. The x' = 0 intercept, 0.35 GeV, is the same as that found in hadron scattering experiments.[10,32]

Conclusions

Within the statistics, Feynman hadronic scaling holds. Furthermore, "unlike" pion-proton (e.g., $\pi^+ + p \rightarrow \pi^- + X$) interactions have similar shapes to virtual photon-proton interactions.

No plateau in rapidity is seen in this data. The rapidity distribution is similar to pion-proton data.

As P_T^2 is varied from 0 to 1.5 GeV^2, the shape of the transverse momentum changes from $\exp(-bP_T^2)$ to $\exp(-bP_T)$.

The function becomes similar to hadronic data from the ISR and Fermilab. The best fit can be made with the function $\exp[-b(P_T^2 + M^2)^{1/2}]$. For high x the estimate is about 1 GeV.

The average transverse momentum increases linearly with x' and then flattens out. The intercept at x' = 0 is the same as that found in hadron scattering data.

No significant variation with q^2 or s has been found in the hadron distributions. Except for the production of more positive than negative hadrons at high x', there is no charge asymmetry in the data.

REFERENCES

1. W. A. Loomis *et al.*, Phys. Rev. Lett. 35, 1483 (1975); other papers in preparation.
2. M. Perl, *High Energy Hadron Physics* (John Wiley, New York, 1974).
3. Jerry Mar *et al.*, Phys. Rev. Lett. 21, 482 (1968).
4. R. E. Taylor, SLAC-PUB-1613, 1975 (unpublished).
5. Chapter 20 of Reference 2.
6. E. D. Bloom *et al.*, Phys. Rev. Lett. 23, 930 (1969); M. Breidenbach *et al.*, 23, 935 (1969); S. Stein *et al.*, Phys. Rev. 12, 1884 (1975).
7. J. D. Bjorken, Phys. Rev. 179, 1547 (1969).
8. R. P. Feynman, *Photon-Hadron Interactions* (Benjamin, New York, 1972).
9. J. D. Bjorken and E. A. Paschos, Phys. Rev. 185, 1975 (1969).
10. P. Capiluppi *et al.*, Nucl. Phys. B79, 189 (1974).
11. L. N. Hand, Phys. Rev. 129, 1834 (1963).
12. J. T. Dakin *et al.*, Phys. Rev. D 10, 1401 (1974).
13. C. F. A. Pantin, Nucl. Phys. B46, 205 (1972).
14. J. T. Dakin and G. J. Feldman, Phys. Rev. D 8, 2862 (1973).
15. R. P. Feynman, ibid, p. 82.
16. Richard P. Feynman, Phys. Rev. Lett. 23, 1415 (1969).
17. Sidney D. Drell and Tung-Mow Yan, Phys. Rev. Lett. 24, 855 (1970); E. W. Colglazier and F. Ravndal, Phys. Rev. D 7, 1537 (1973).

18. J. Bjorken, in the *Proceedings of the 1971 International Symposium on Electron and Photon Interactions at High Energies,* (Cornell, Ithaca, 1972).

19. S. M. Berman, J. D. Bjorken, and J. B. Kogut, Phys. Rev. D 4, 3388 (1971); H. D. I. Abarbanel and J. B. Kogut, Phys. Rev. D 5, 2050 (1972); H. Cheng and T. T. Wu, Phys. Rev. Lett. 22, 1409 (1969).

20. R. Hagedorn, Nucl. Phys. B24, 93 (1970); and earlier papers cited in that reference.

21. K. B. Burns *et al.*, Nucl. Instr. and Meth. 106, 171 (1973).

22. T. A. Nunamaker, Rev. Sci, Instr. 42, 1701 (1971); T. A. Nunamaker, Nucl. Instr. and Methods 106, 557 (1973).

23. L. W. Mo and Y. Tsai, Rev. Mod. Phys. 41, 247 (1969).

24. J. Ballam *et al.*, paper submitted to the XVI International Conference on High Energy Physics, Chicago and Batavia, Illinois, also SLAC-PUB-1163, 1972 (unpublished).

25. V. Eckardt *et al.*, DESY Report 74/5, 1974 (unpublished); G. Wolf, DESY Report 75/40, 1975 (unpublished).

26. C. A. Heusch, in the proceedings of the *XVII International Conference on High Energy Physics* (Rutherford, London, 1974); see also M. L. Perl's talk in those proceedings.

27. C. J. Bebek *et al.*, Phys. Rev. Lett. 32, 27 (1973).

28. J. Whitmore, Phys. Rep. 10C, 273 (1974); P. T. Go *et al.*, Phys. Rev. D 11, 3092 (1975).

29. V. P. Kenney *et al.*, to be published.

30. K. Berkelman, Acta Phys. Polon. 6, 751 (1974).

31. J. W. Cronin *et al.*, Phys. Rev. D 11, 3105 (1975).

32. G. W. van Apeldoorn *et al.*, Nucl. Phys. B91, 1 (1975); A. M. Rossi *et al.*, Nucl. Phys. B84, 3 (1975).

TABLE 1

INEFFICIENCY IN HADRON IDENTIFICATION BY CUTS

Cut	Inefficiency--%
1) Out of time tracks	1.69
2) Downstream track misses vertex in y	1.34
3) No link to x track	8.36
4) No link to y track	18.31
5) Linked track misses vertex	2.82

TABLE 2

EXPERIMENTS ON HADRON PRODUCTION FROM LEPTON-PROTON SCATTERING

Experiment	Lepton	S (GeV^2) range	q^2 (GeV^2) range
SLAC hybrid bubble chamber[a]	μ^-	2-16	0.15-2.0
DESY streamer chamber[b]	e^-	1.7-7.8	0.3 -1.5
SLAC-Santa Cruz streamer chamber[c]	μ^+	2-4	0.3 -1.3
Harvard-Cornell double arm spectrometer[d]	e^-	4.6-7	0.6 -1.2
SLAC forward spectrometer[e]	e^-	12-30	0.25-3.0
Chicago-Harvard-Illinois-Oxford forward spectrometer--this experiment	μ^+	20-270	0.5 -50.

[a] Ref. 24

[b] Ref. 25

[c] Ref. 26

[d] Ref. 27

[e] Ref. 12

TABLE 3

$G(P_T^2)$--TRANSVERSE MOMENTUM DISTRIBUTIONS

Fits to $\exp(-bP_T^2)$; $P_T^2 < 0.54$ GeV^2

			b (GeV^{-2})	Δb (GeV^{-2})	χ^2/DF
Lo s	Lo x'	-	4.47	.74	.64
Lo s	Lo x'	+	4.48	.65	.92
Lo s	Hi x'	-	3.59	1.31	2.11
Lo s	Hi x'	+	2.36	1.35	.19
Hi s	Lo x'	-	5.39	.24	3.04
Hi s	Lo x'	+	5.72	.23	2.74
Hi s	Hi x'	-	4.12	.70	.35
Hi s	Hi x'	+	4.23	1.32	.20

Fits to $\exp(-bP_T)$

			b (GeV^{-1})	Δb (GeV^{-1})	χ^2/DF
Lo s	Lo x'	-	4.75	.29	1.05
Lo s	Lo x'	+	4.61	.29	3.04
Lo s	Hi x'	-	3.13	.50	1.72
Lo s	Hi x'	+	3.00	.40	.75
Hi s	Lo x'	-	4.82	.08	2.53
Hi s	Lo x'	+	5.06	.08	4.50
Hi s	Hi x'	-	3.71	.23	.37
Hi s	Hi x'	+	3.26	.34	.63

Fits to $\exp[-b(P_T^2 + M^2)^{1/2}]$

			b (GeV^{-1})	Δb (GeV^{-1})	M (GeV)	ΔM (GeV)	χ^2/DF
Lo s	Lo x'	-	7.61	1.01	.64	.15	.59
Lo s	Lo x'	+	8.79	.29	.71	.06	1.75
Lo s	Hi x'	-	6.17	.69	.98	.14	1.69
Lo s	Hi x'	+	5.89	.32	1.00	.21	1.06
Hi s	Lo x'	-	6.01	.38	.34	.06	1.25
Hi s	Lo x'	+	6.69	.42	.41	.07	1.60
Hi s	Hi x'	-	6.69	.66	.83	.02	.71
Hi s	Hi x'	+	5.69	.64	1.03	.08	.77

Lo s $20 < s < 100$ GeV^2	Lo x' $0.04 < x' < 0.5$	+ positive hadrons
Hi s $s > 100$ GeV^2	Hi x' $0.50 < x' < 1.0$	- negative hadrons

Figure 1. The one-photon exchange Feynman diagram for the reaction $\ell + N \rightarrow \ell' + h + X$.

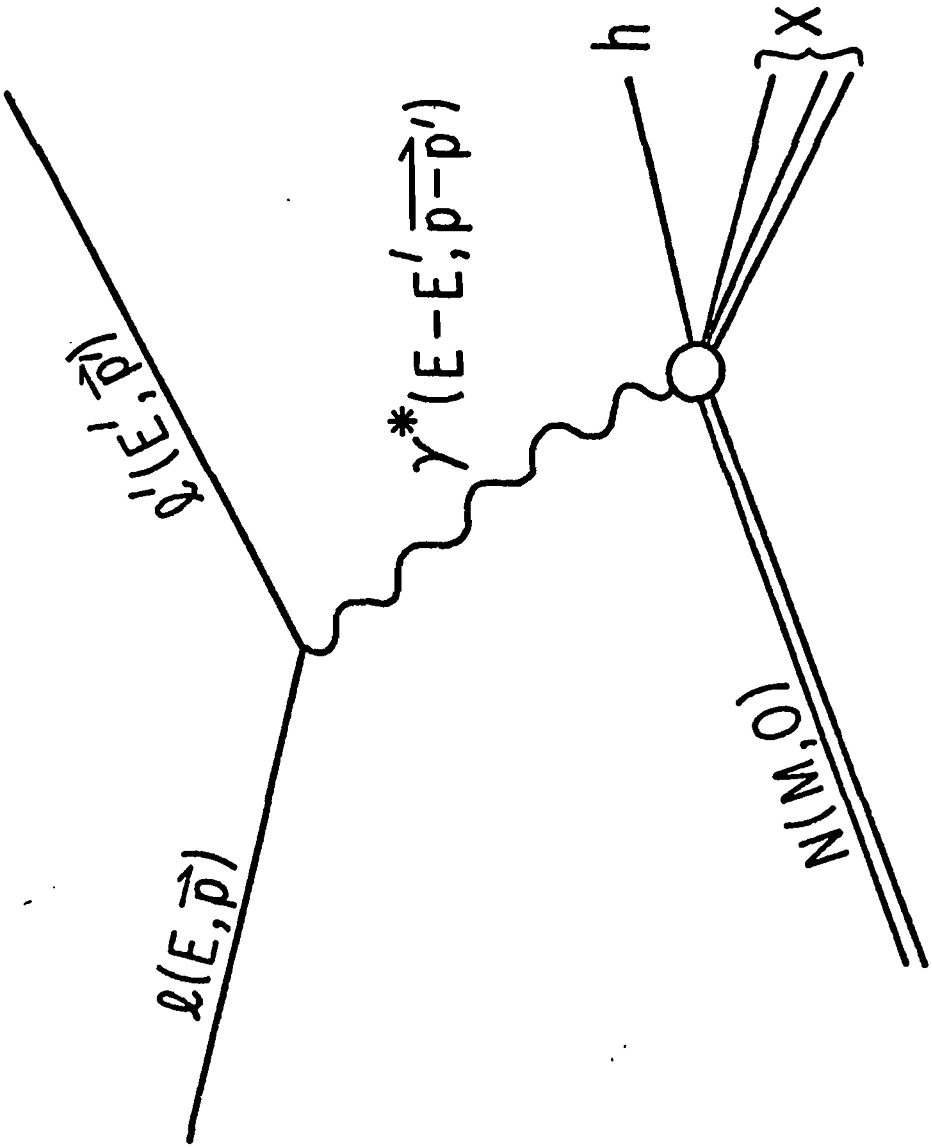
ℓ(E,$\vec{p}$)
ℓ′(E′,$\vec{p}'$)
γ*(E−E′,$\overrightarrow{p-p'}$)
h
X
N(M,0)

Figure 2. Parton model picture of the interaction of a virtual photon with a nucleon. a) Before the interaction--the virtual photon is on the left and the partons which form the nucleon are on the right. b) After the interaction--one parton has been struck by the virtual photon and kicked away from the other partons. The rest of the nucleon is undisturbed except for the missing parton.

(a)

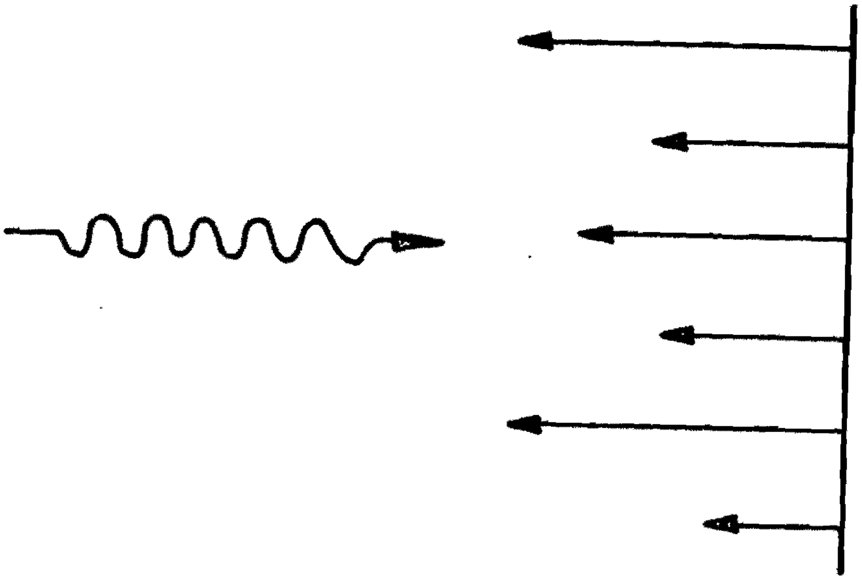

(b)

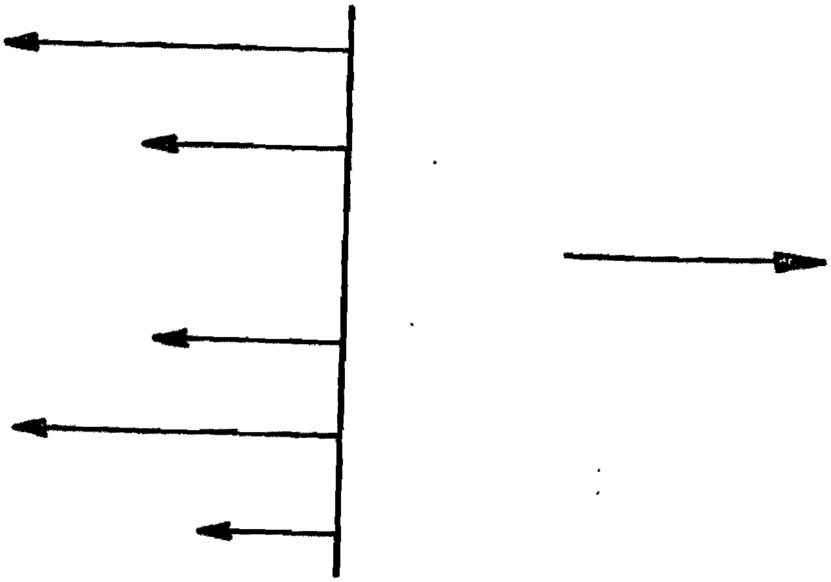

Figure 3. Parton rapidity distribution for a γ^* - N interaction. a) Rapidity distribution of the nucleon before the interaction. b) One parton has its rapidity increased by absorbing the virtual photon. A hole (indicated by the dotted lines) is created in the rapidity distribution of the nucleon. c) The struck parton and the remaining partons in the nucleon fragment into particles. The rapidity distribution becomes smeared.

(a)

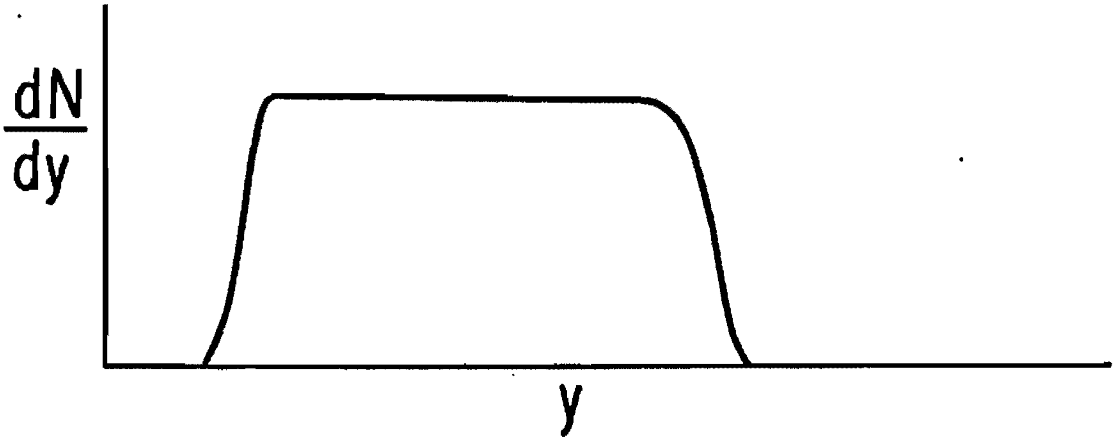

(b)

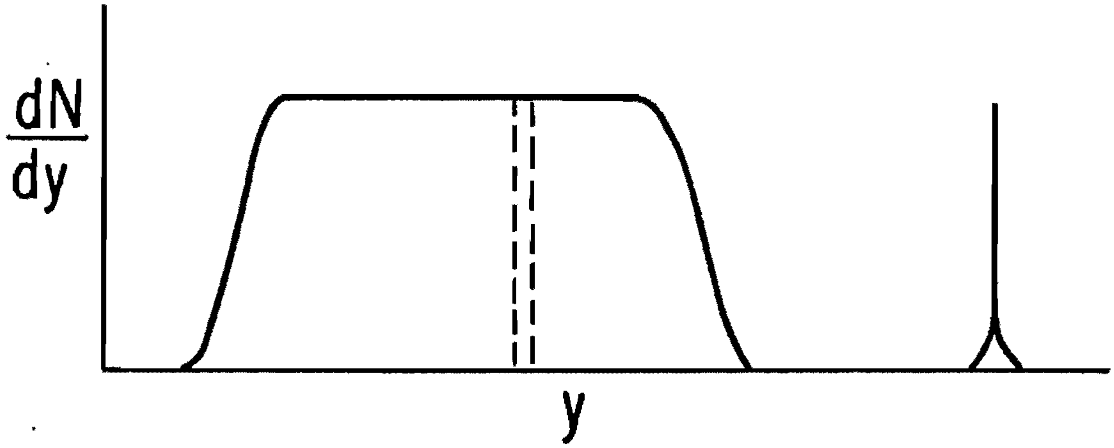

(c)

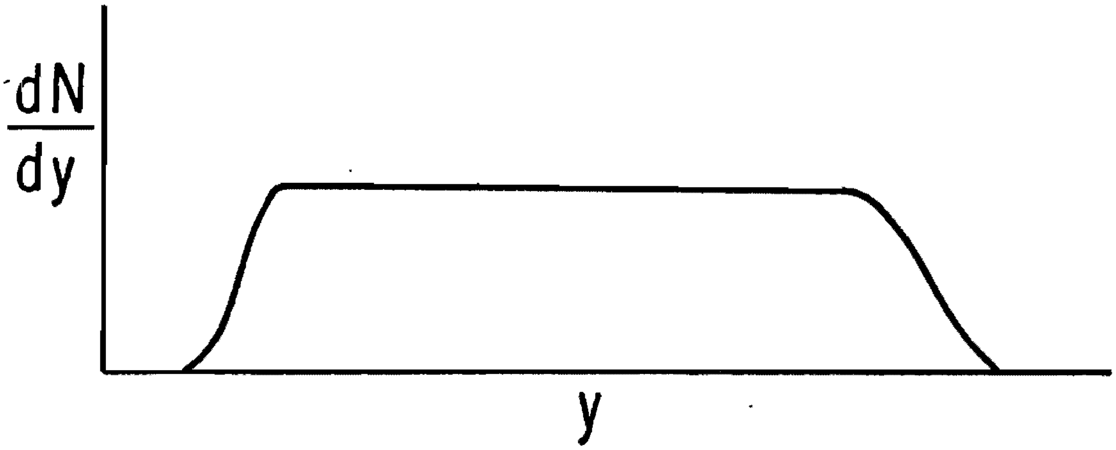

Figure 4. Diagram of the apparatus. S0-4 are wire chambers, 1E4 is a magnet, LH is the liquid hydrogen target, A is the steel hadron absorber, and B, H, G, N, M, and M' are counters.

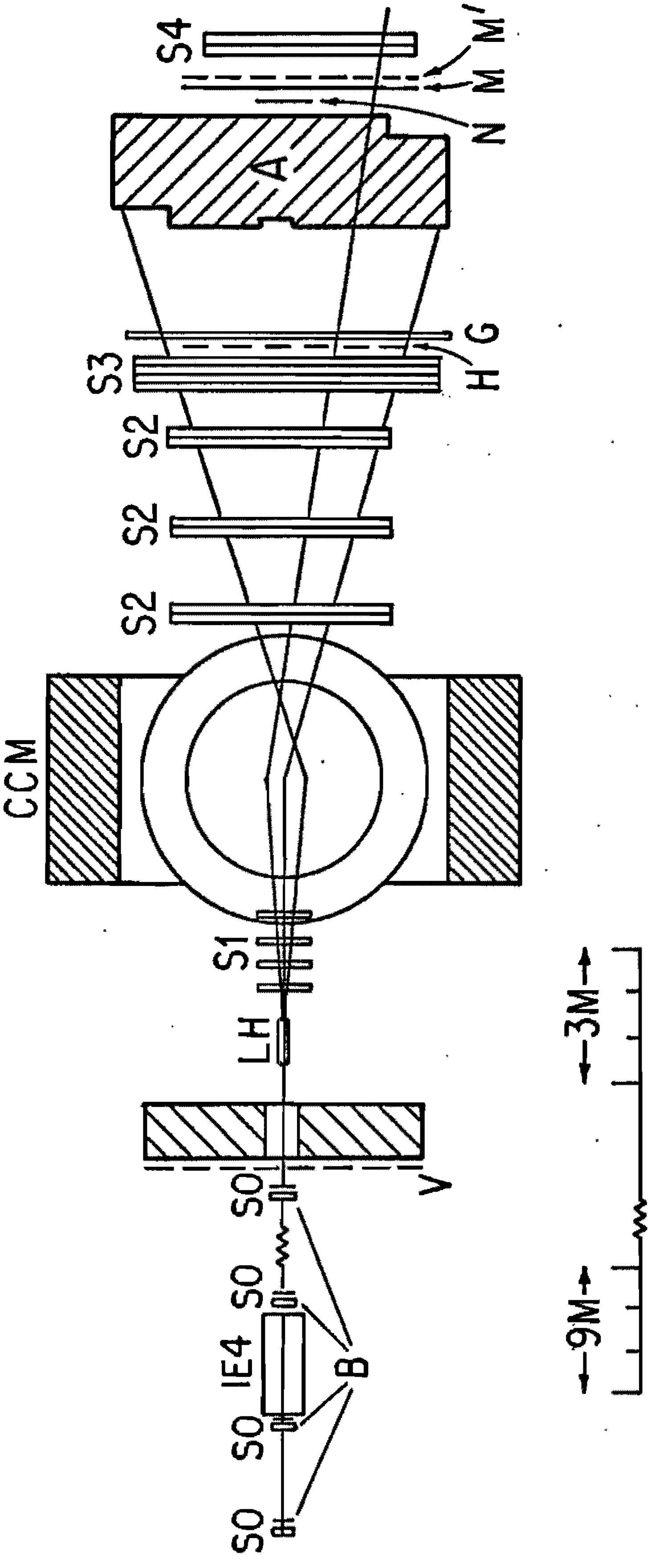
S4
M'
M
N
A
G
H
S3
S2
S2
S2
CCM
S1
LH
V
SO
SO
SO
SO
IE4
B
3M
9M

Figure 5. Muon beam line. T0 is the aluminum target for production of kaons and pions. D0-3 are dipole magnets and Q0-2 are quadrupoles.

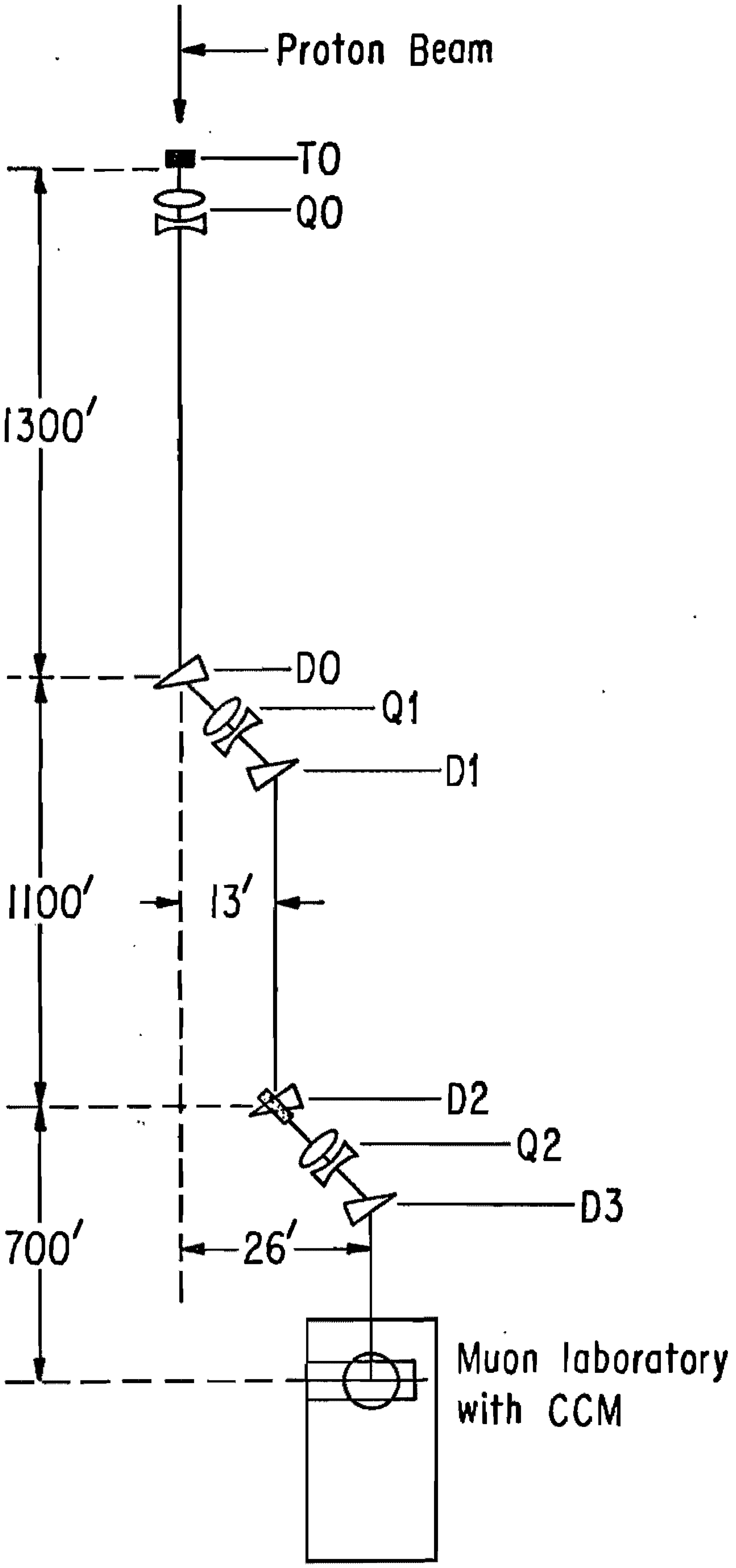
Proton Beam
T0
Q0
1300′
D0
Q1
D1
1100′
13′
D2
Q2
D3
700′
26′
Muon laboratory
with CCM

Figure 6. x linking error for tracks upstream and downstream of the CCM. The difference of the upstream and downstream impact parameter is histogrammed.

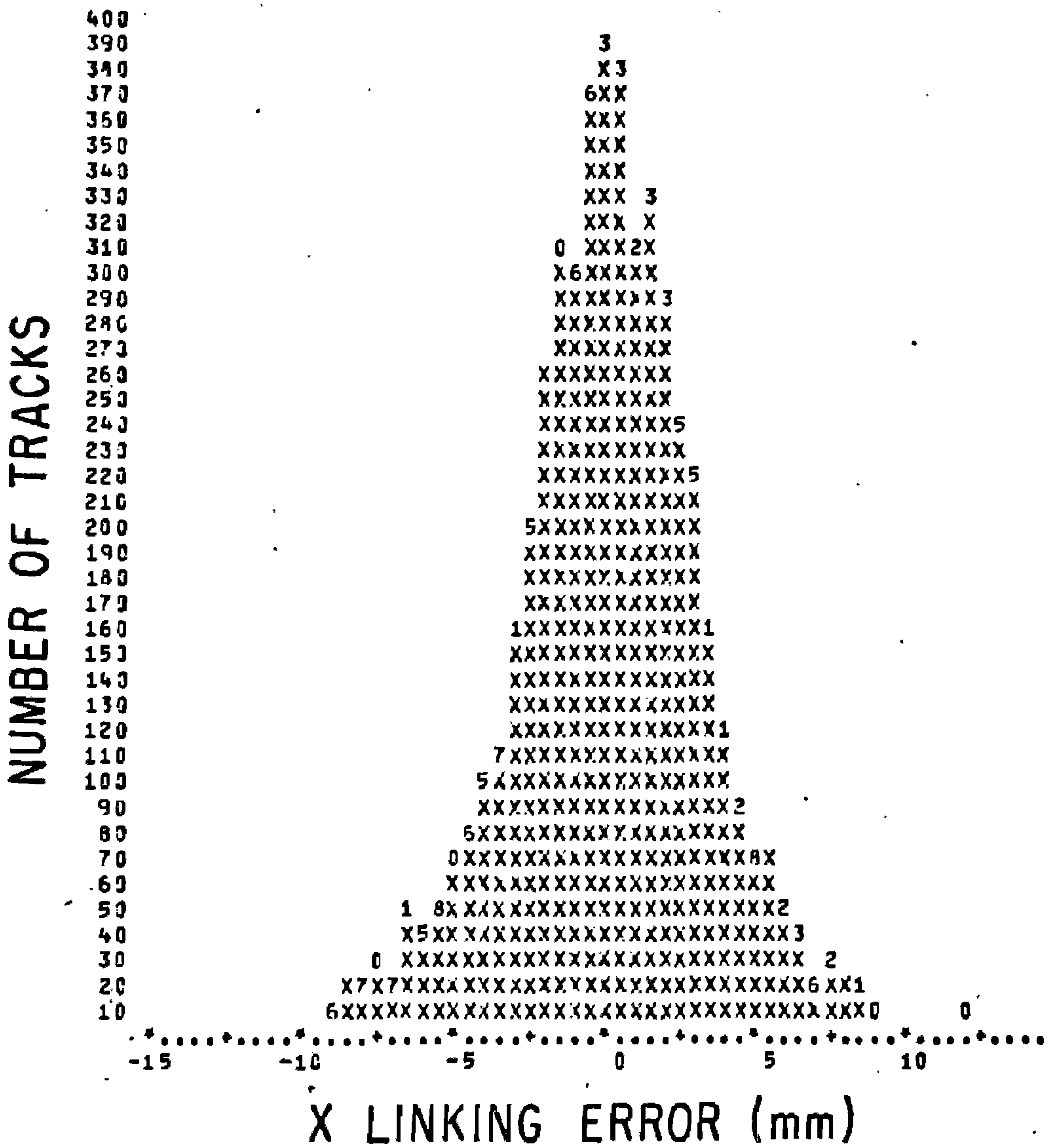
NUMBER OF TRACKS
400
390
380
370
360
350
340
330
320
310
300
290
280
270
260
250
240
230
220
210
200
190
180
170
160
150
140
130
120
110
100
90
80
70
60
50
40
30
20
10
-15
-10
-5
0
5
10
X LINKING ERROR (mm)

Figure 7. Reconstructed vertex for events with $q^2 > 0.5$ GeV^2 and $s > 20$ GeV^2. Events where the muon scattered from the last beam hodoscope, the upstream target window, and the LH_2 target can clearly be identified.

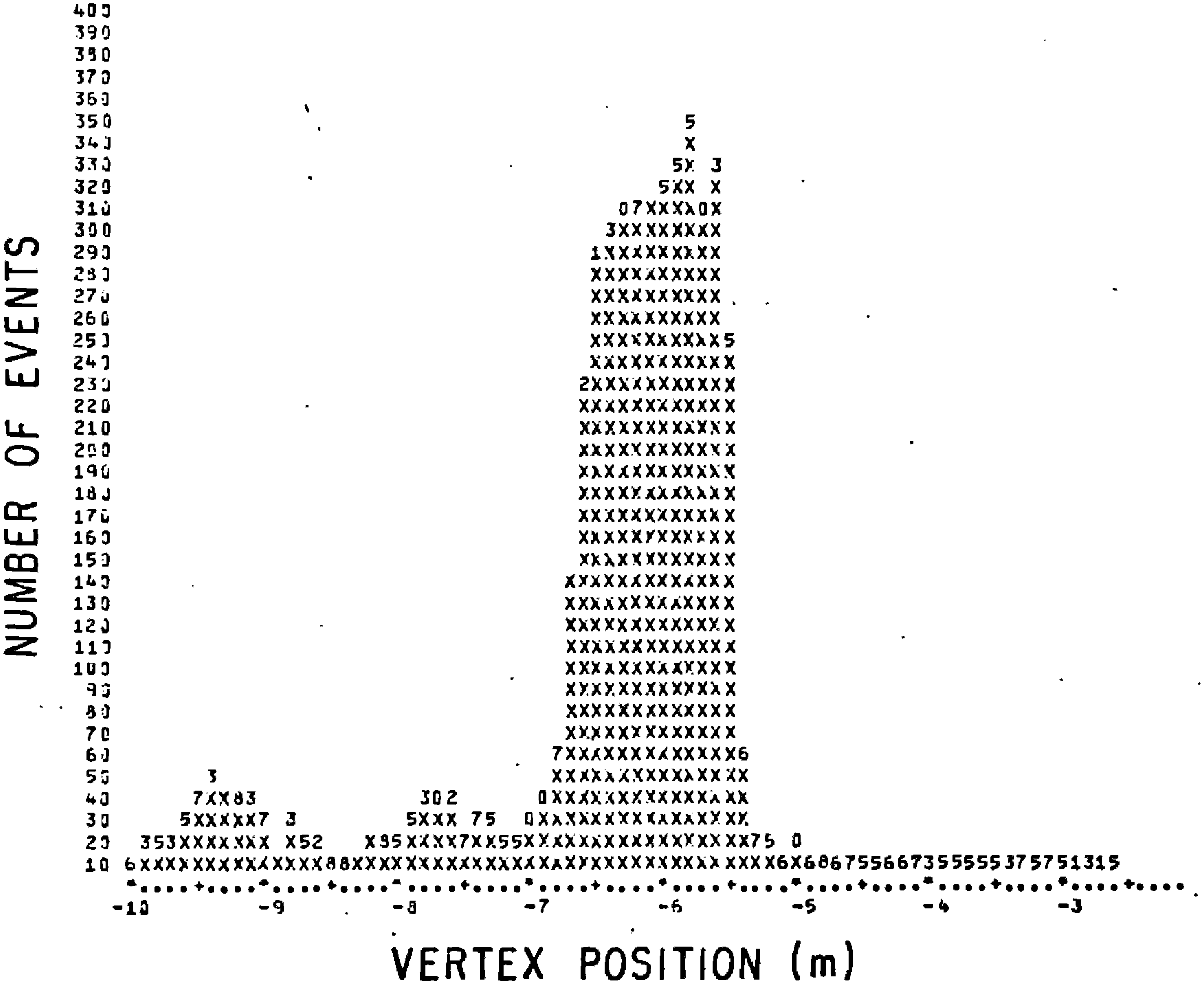
NUMBER OF EVENTS
VERTEX POSITION (m)
400
390
380
370
360
350
340
330
320
310
300
290
280
270
260
250
240
230
220
210
200
190
180
170
160
150
140
130
120
110
100
90
80
70
60
50
40
30
20
10
-10
-9
-8
-7
-6
-5
-4
-3

Figure 8. Excess energy for muon-proton events. Excess energy is defined as the sum of the energy detected minus the energy of the incident muon. 22 events have excess energy greater than 170 GeV, the upper limit shown on the histogram.

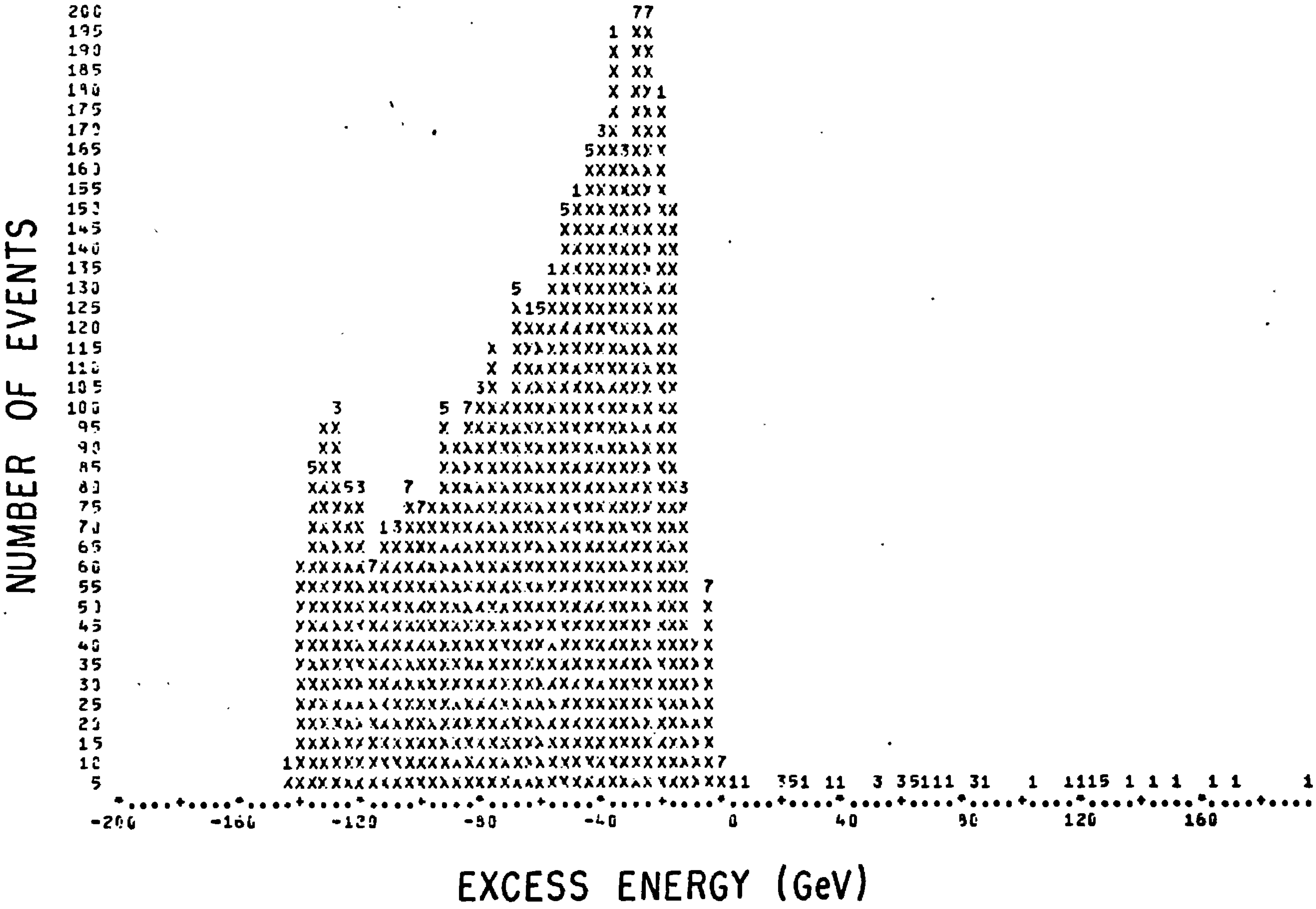
NUMBER OF EVENTS
200
195
190
185
180
175
170
165
160
155
150
145
140
135
130
125
120
115
110
105
100
95
90
85
80
75
70
65
60
55
50
45
40
35
30
25
20
15
10
5
-200
-160
-120
-80
-40
0
40
80
120
160
EXCESS ENERGY (GeV)

Figure 9. Intercepts of the tracks of hadrons at the 6m chambers. Each circle represents the projections of particles with the same transverse momentum. The circles in each figure have the same longitudinal momentum. Hadrons whose projections do not intercept the chambers have no acceptance. Some circles in a) and c) do not intersect the chambers so there exists some values of P_L and P_T that can not be detected. Since all the circles in b) intercept the chambers, all values of P_T can be detected.

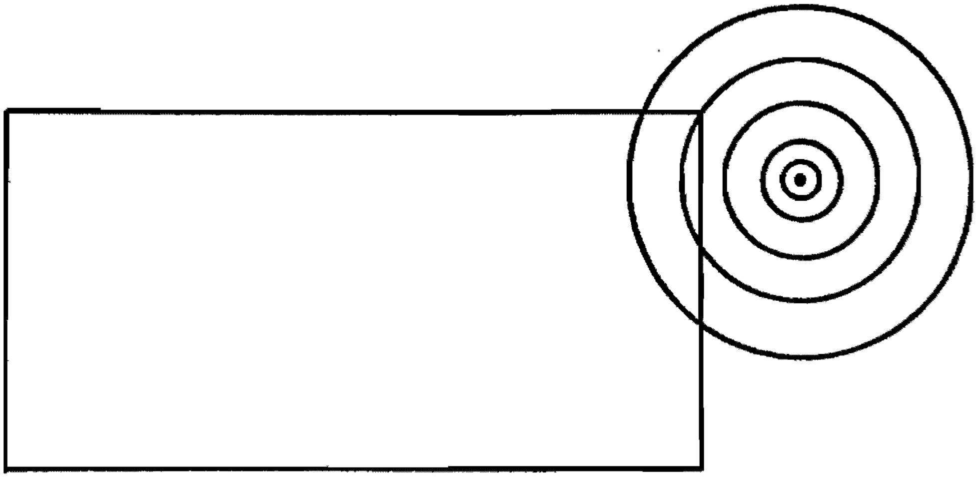

(a)

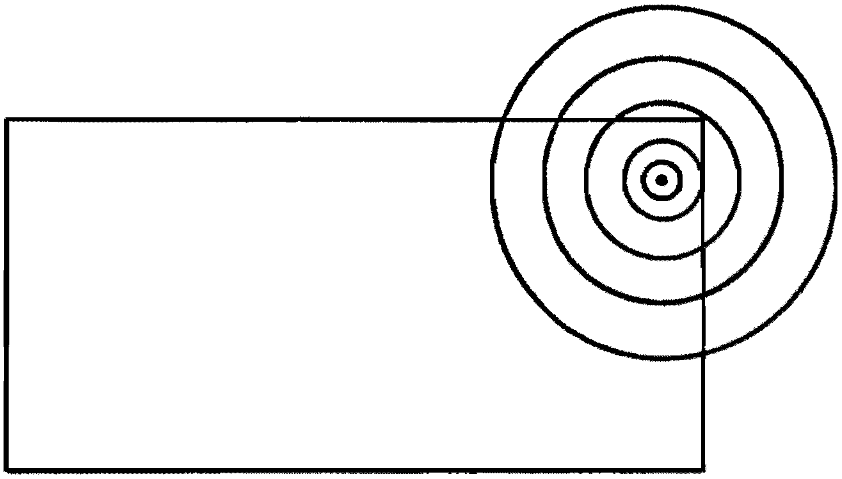

(b)

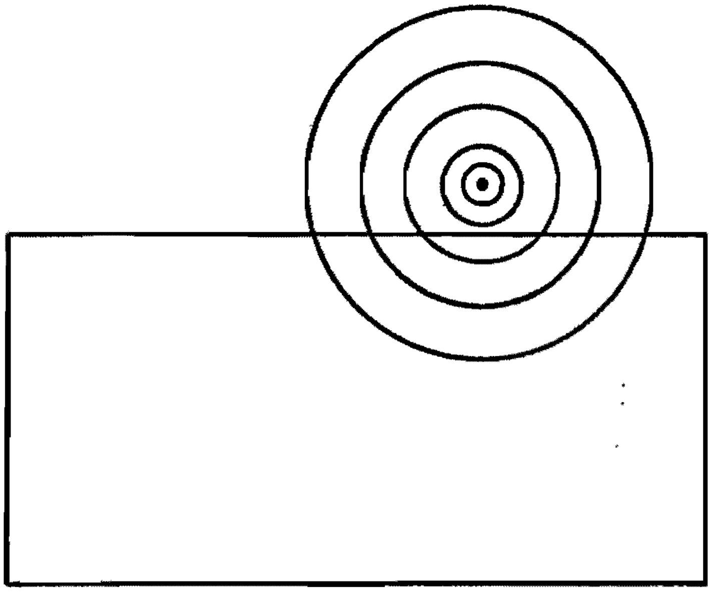

(c)

Figure 10. Contours of constant muon acceptance for 150 GeV muons.

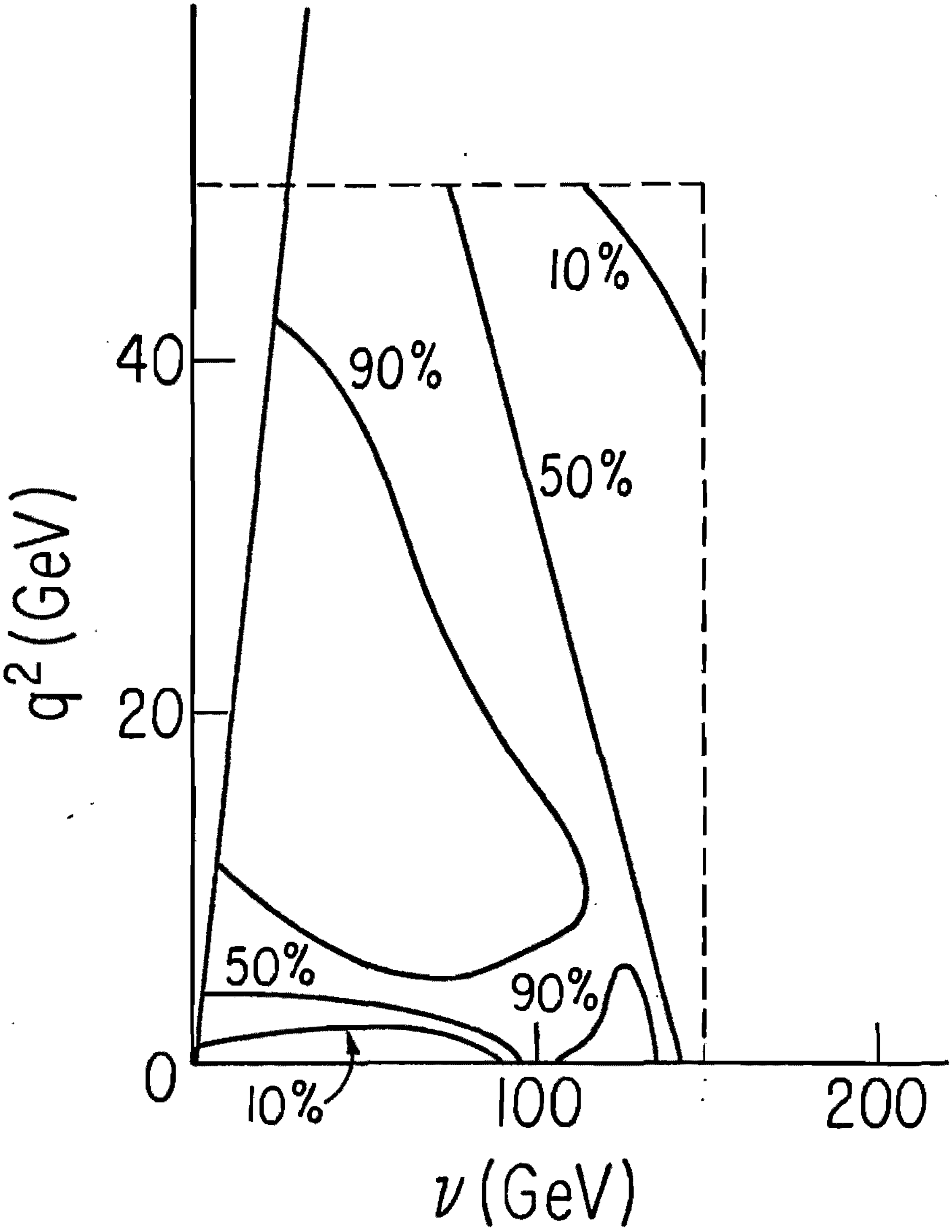
10%
90%
50%
40
20
0
q^2 (GeV)
50%
90%
10%
100
200
ν (GeV)

Figure 11. $q^2 - \nu$ scatter plots for events which survived the cuts. The only difference between the two scatter plots is the q^2 scale. 4 events have q^2 greater than 50 GeV^2. Each symbol represents the number of events in a bin. 1 to 31 events are represented by the symbols +, 2-9, A-U respectively; more than 31 events are indicated by the symbol V.

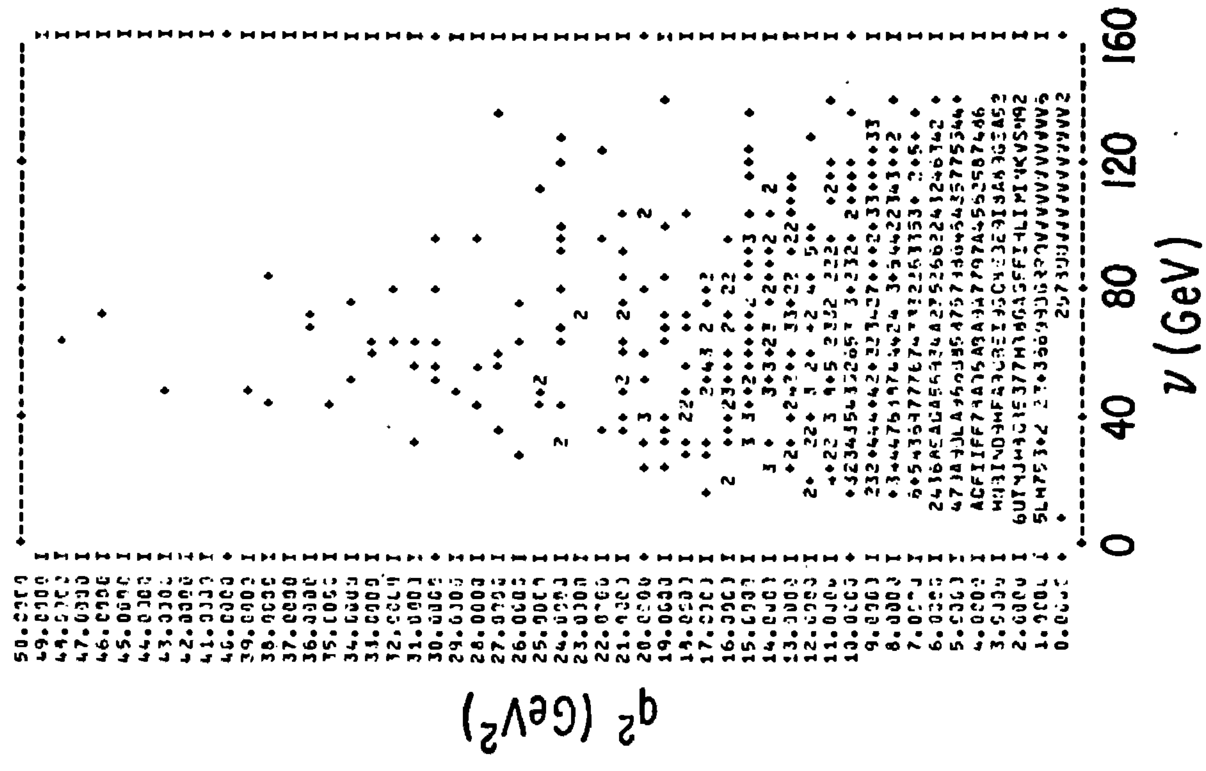
q² (GeV²)
ν (GeV)
0
40
80
120
160
0.0000
10.0000
20.0000
30.0000
40.0000
50.0000

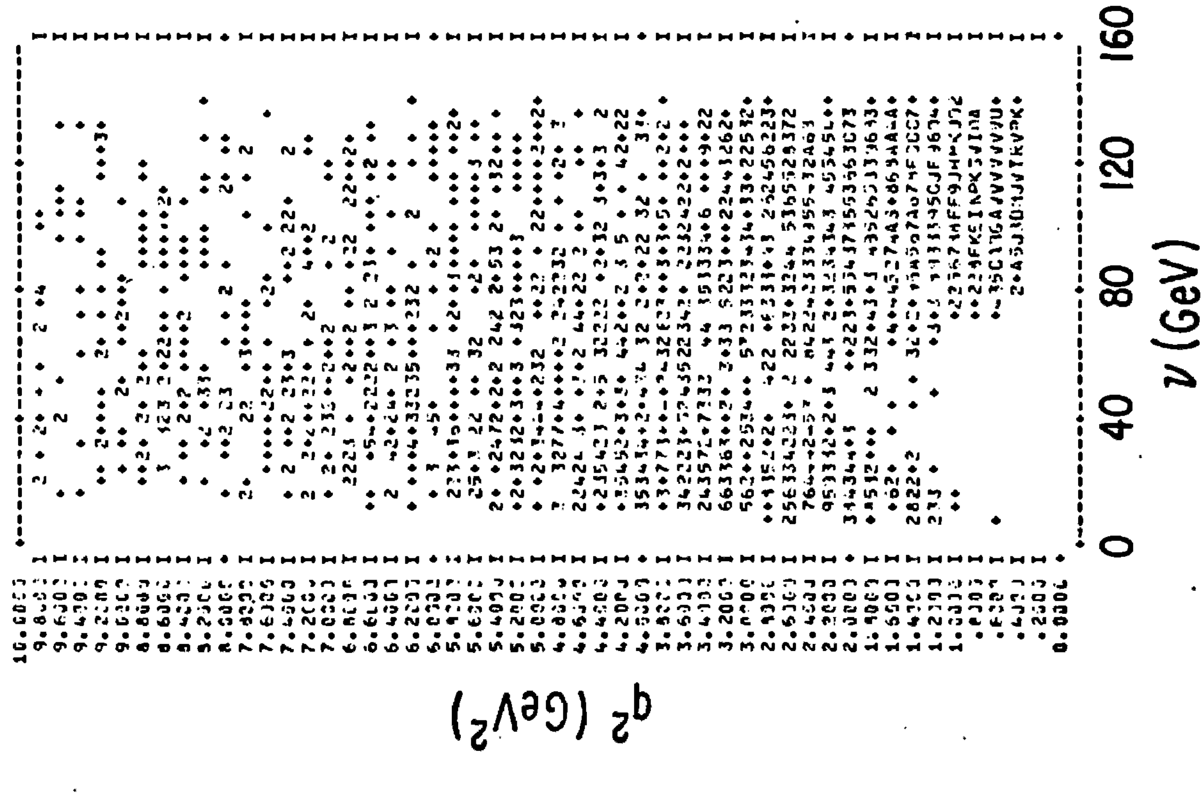
q² (GeV²)
ν (GeV)
0
40
80
120
160
0.0000
2.0000
4.0000
6.0000
8.0000
10.0000

Figure 12. Invariant longitudinal momentum spectrum for charged inclusive hadrons in several intervals of q^2 and s. The dotted line is 0.34 exp(−3.4 x'). A and D contain events in the range $0.5 < q^2 < 3.0$; B and E, $3 < q^2 < 10$; C and F, $q^2 > 10$.

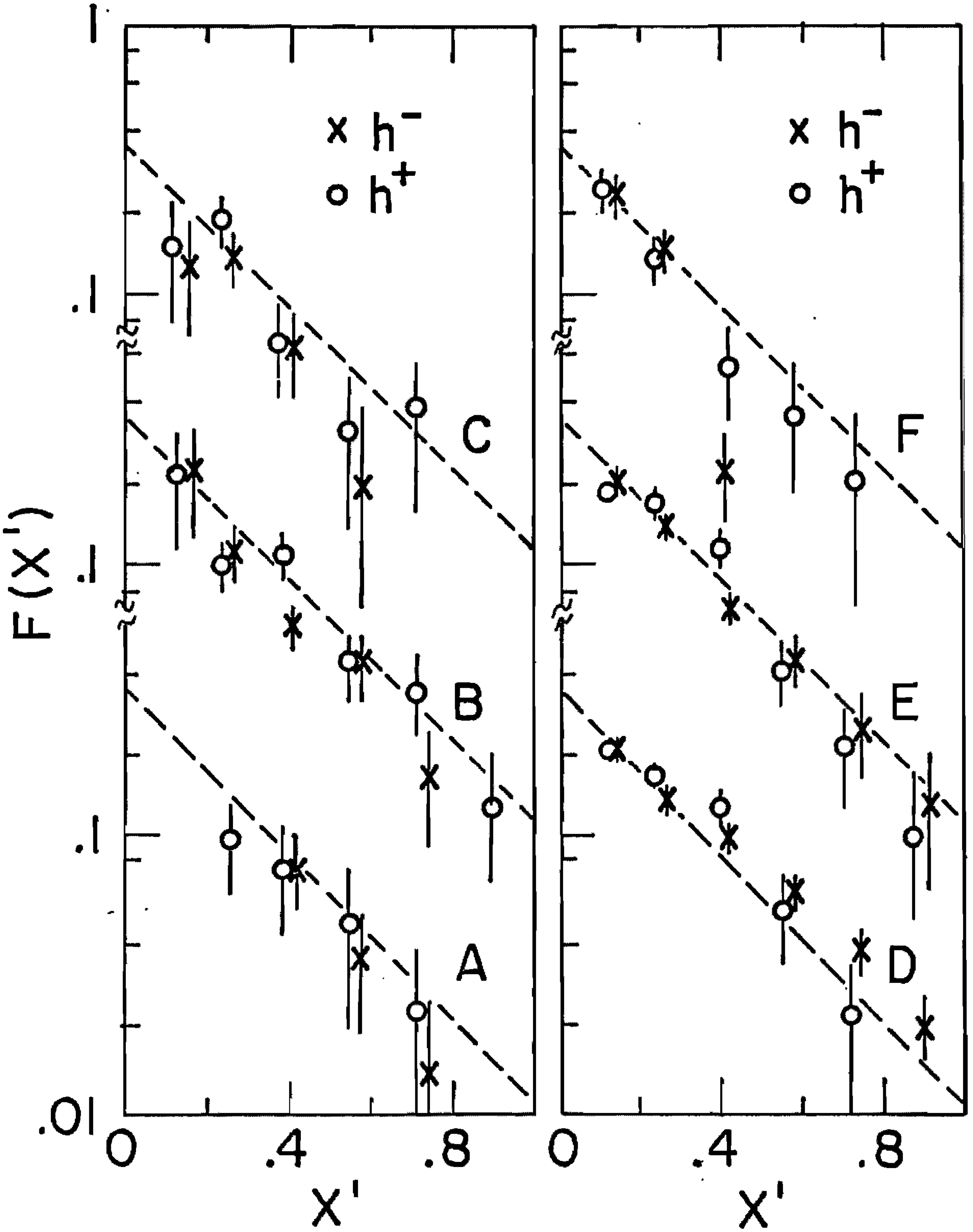
x h⁻
o h⁺
x h⁻
o h⁺
1
.1
.1
.1
.01
F(X')
A
B
C
D
E
F
0
.4
.8
0
.4
.8
X'
X'

Figure 13. Comparison of F(x') measured in this experiment (E in Figure 12) with F(x') found from various hadron scattering experiments. The hadron data is from reference 28. Measurements of $\pi - p$ were done at $s = 36\ \text{GeV}^2$; measurements of $p - p$ were done at $386\ \text{GeV}^2$.

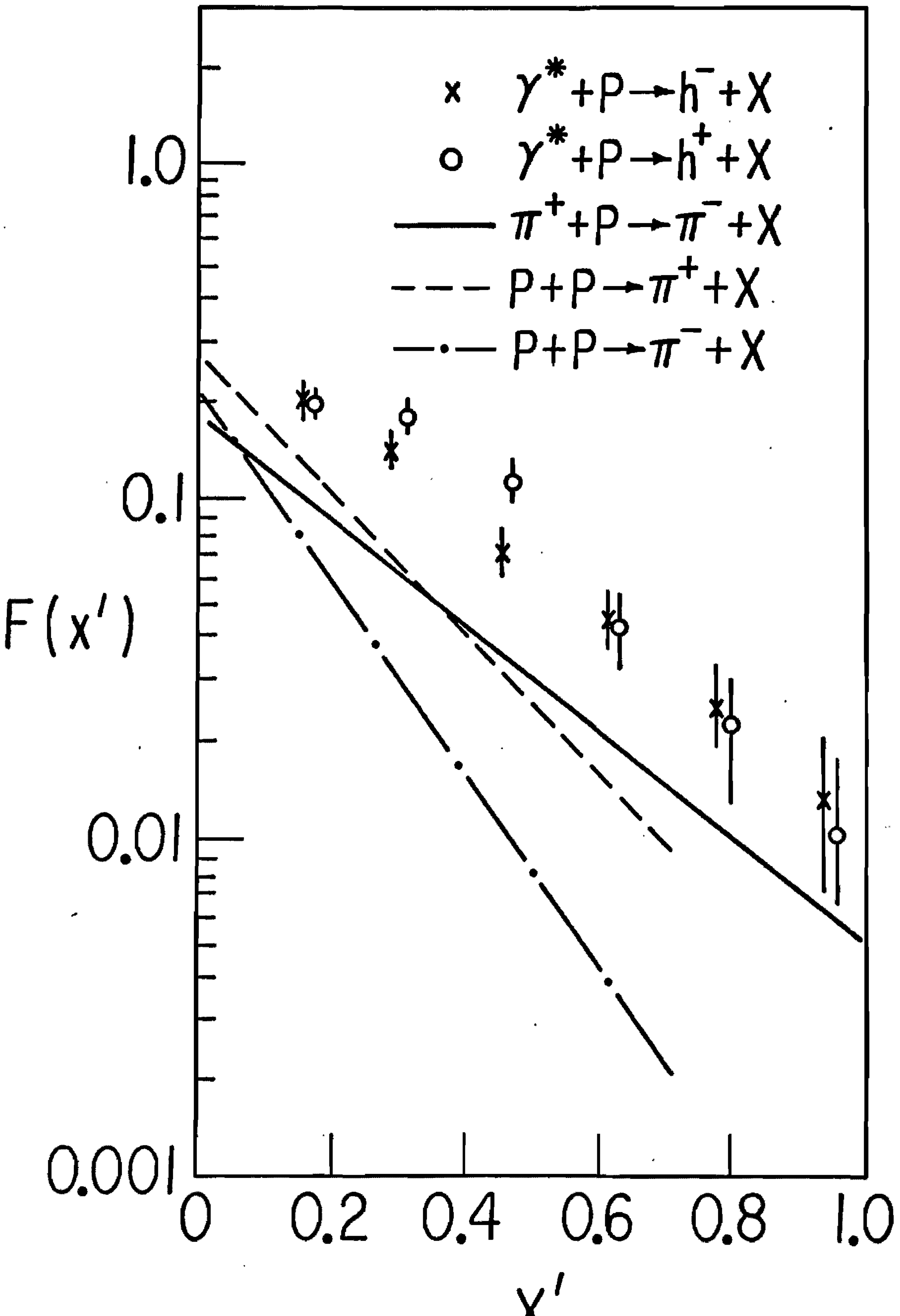
× $\gamma^* + P \to h^- + X$
○ $\gamma^* + P \to h^+ + X$
$\pi^+ + P \to \pi^- + X$
$P + P \to \pi^+ + X$
$P + P \to \pi^- + X$
1.0
0.1
0.01
0.001
F(x')
0
0.2
0.4
0.6
0.8
1.0
X'

Figure 14. Rapidity distributions for events within the range $20 < s < 100$ GeV^2. The pion scattering data is from reference 29.

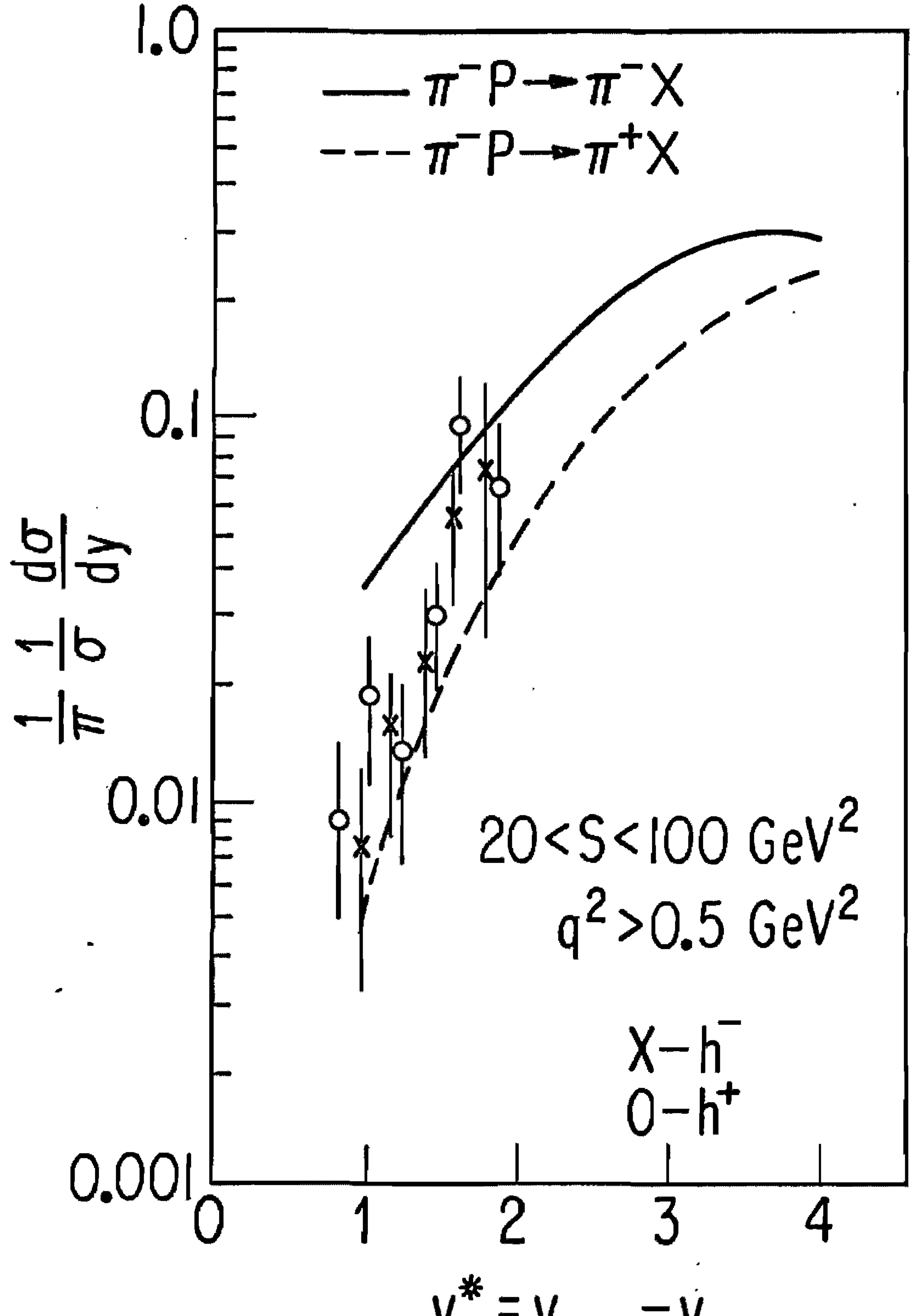

$\pi^- P \to \pi^- X$
$\pi^- P \to \pi^+ X$
$\frac{1}{\pi}\frac{1}{\sigma}\frac{d\sigma}{dy}$
1.0
0.1
0.01
0.001
0
1
2
3
4
$y^* = y_{max} - y$
$20 < S < 100$ GeV^2
$q^2 > 0.5$ GeV^2
X–h^-
O–h^+

Figure 15. Rapidity distributions for events with $s > 100\ \mathrm{GeV}^2$. The pion scattering data is from reference 29.

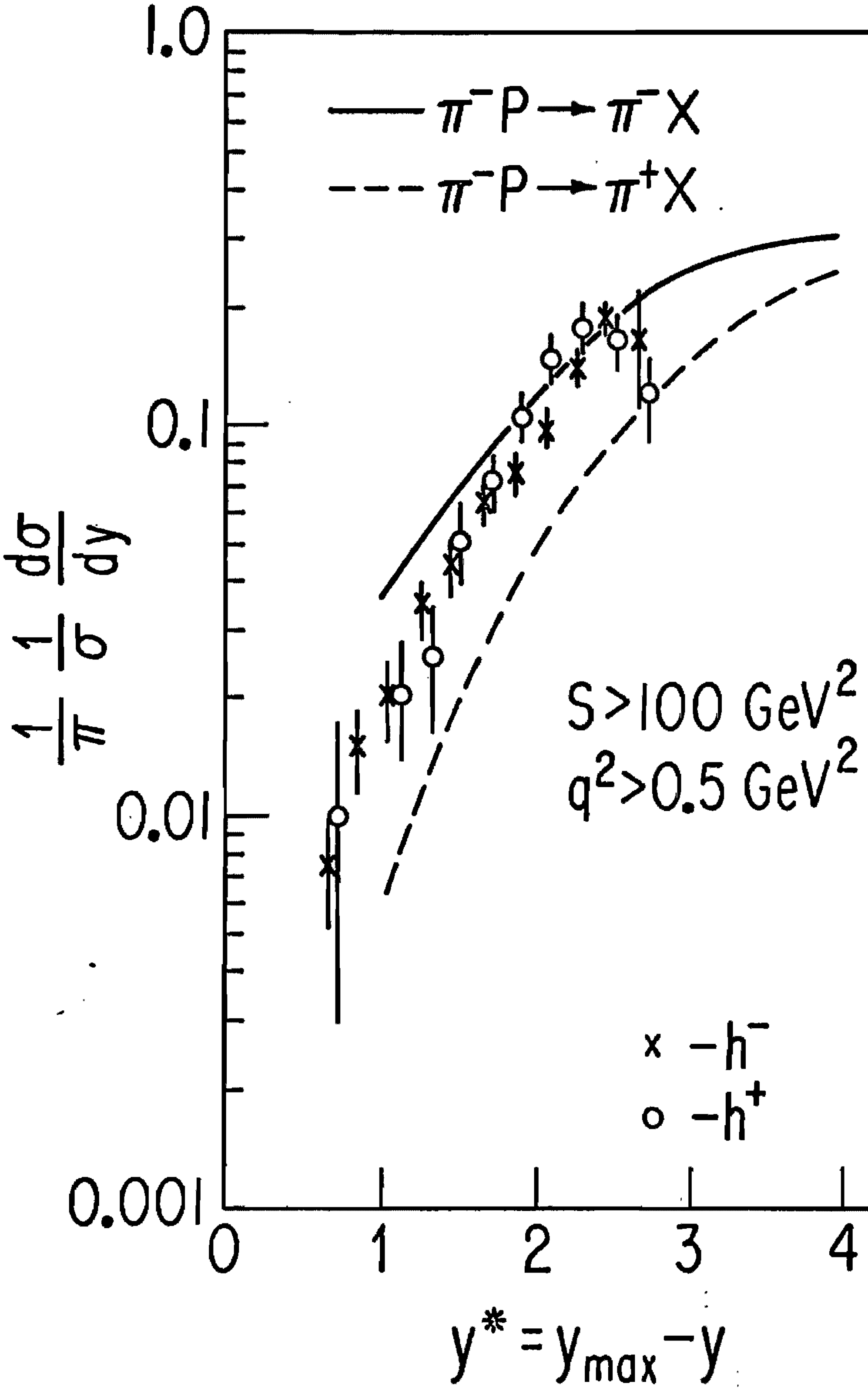
1.0
0.1
0.01
0.001
$\frac{1}{\pi}\frac{1}{\sigma}\frac{d\sigma}{dy}$
$\pi^-P \rightarrow \pi^-X$
$\pi^-P \rightarrow \pi^+X$
$S > 100\ GeV^2$
$q^2 > 0.5\ GeV^2$
x $-h^-$
o $-h^+$
0
1
2
3
4
$y^* = y_{max} - y$

Figure 16. Ratio of positive to negative charged hadrons as a function of q^2, s, and x'. The q^2 intervals are the same as those in Figure 12.

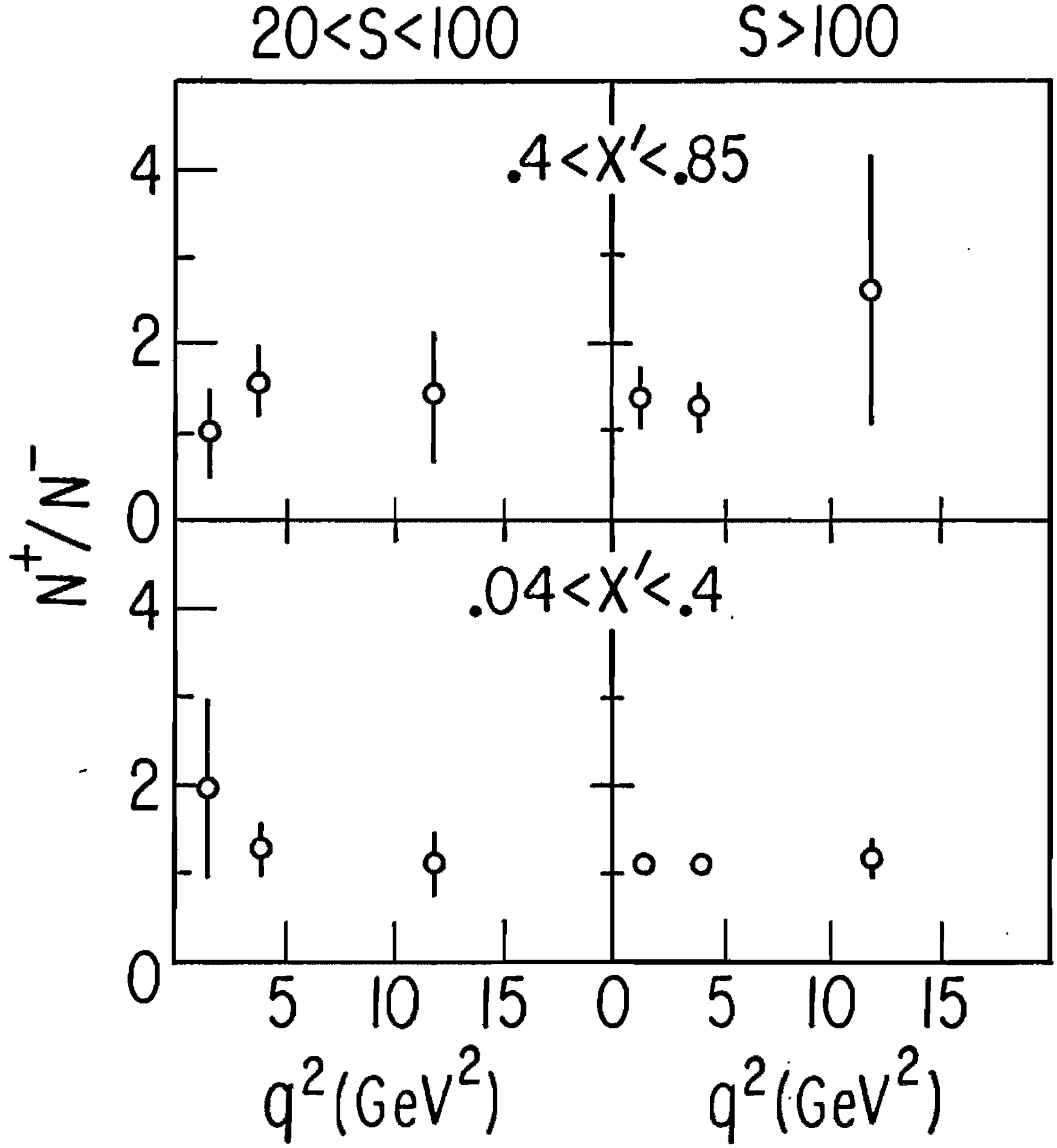
20<S<100
S>100
.4<X'<.85
.04<X'<.4
N^+/N^-
4
2
0
4
2
0
5
10
15
0
5
10
15
q^2(GeV^2)
q^2(GeV^2)

Figure 17. Charge ratio test of the Dakin-Feldman quark-parton model. The points from Bebek *et al.* and Dakin *et al.* are taken from references 27 and 12 respectively. All points are in the range $0.4 < x' < 0.85$.

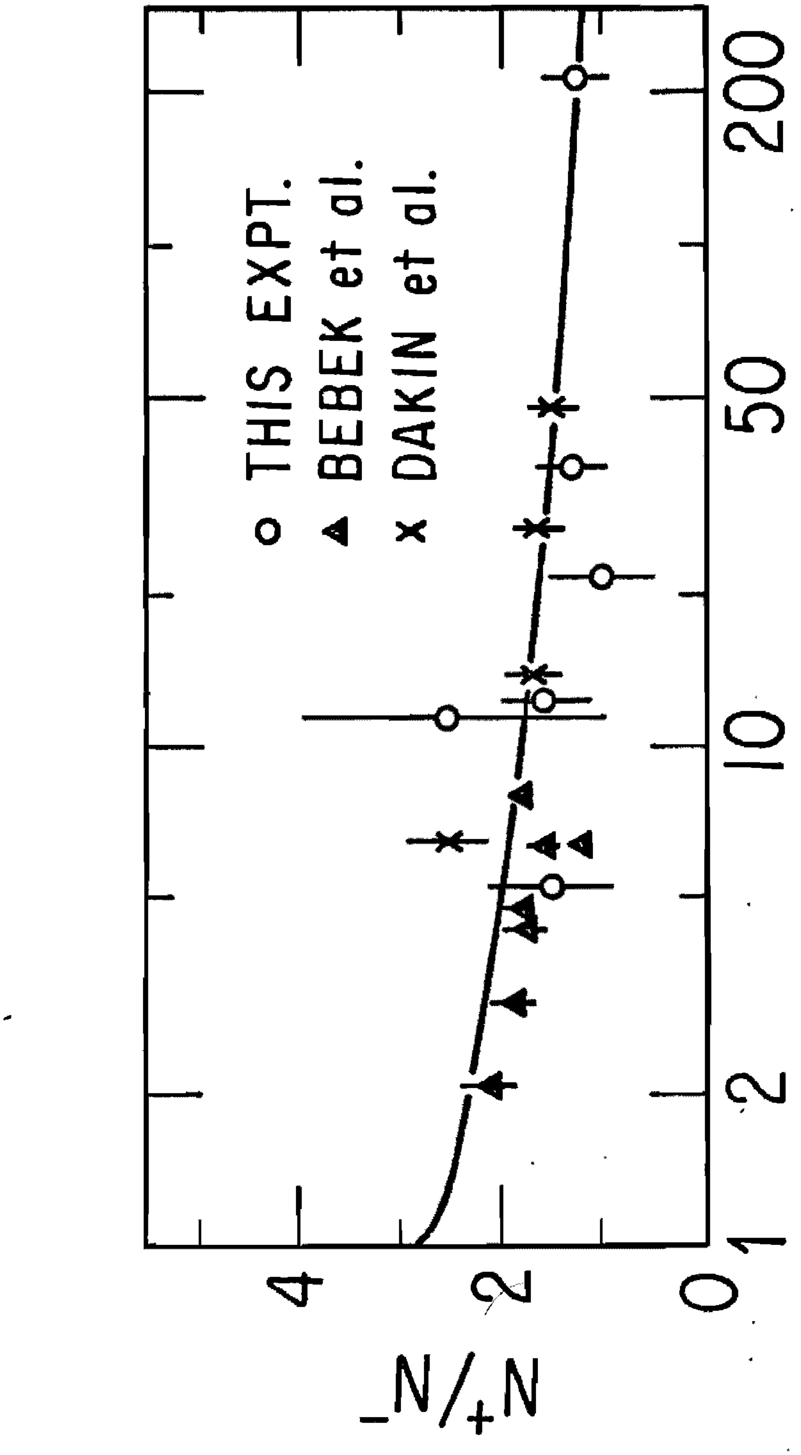
○ THIS EXPT.
▲ BEBEK et al.
× DAKIN et al.
N^+/N^-
0
2
4
1
2
10
50
200
ω

Figure 18. $G(P_T^2)$, the hadron transverse momentum distribution, fit to $\exp(-bP_T^2)$, for hadrons that have P_T^2 less than 0.54 GeV^2. The q^2 intervals are the same as those used in Figure 12.

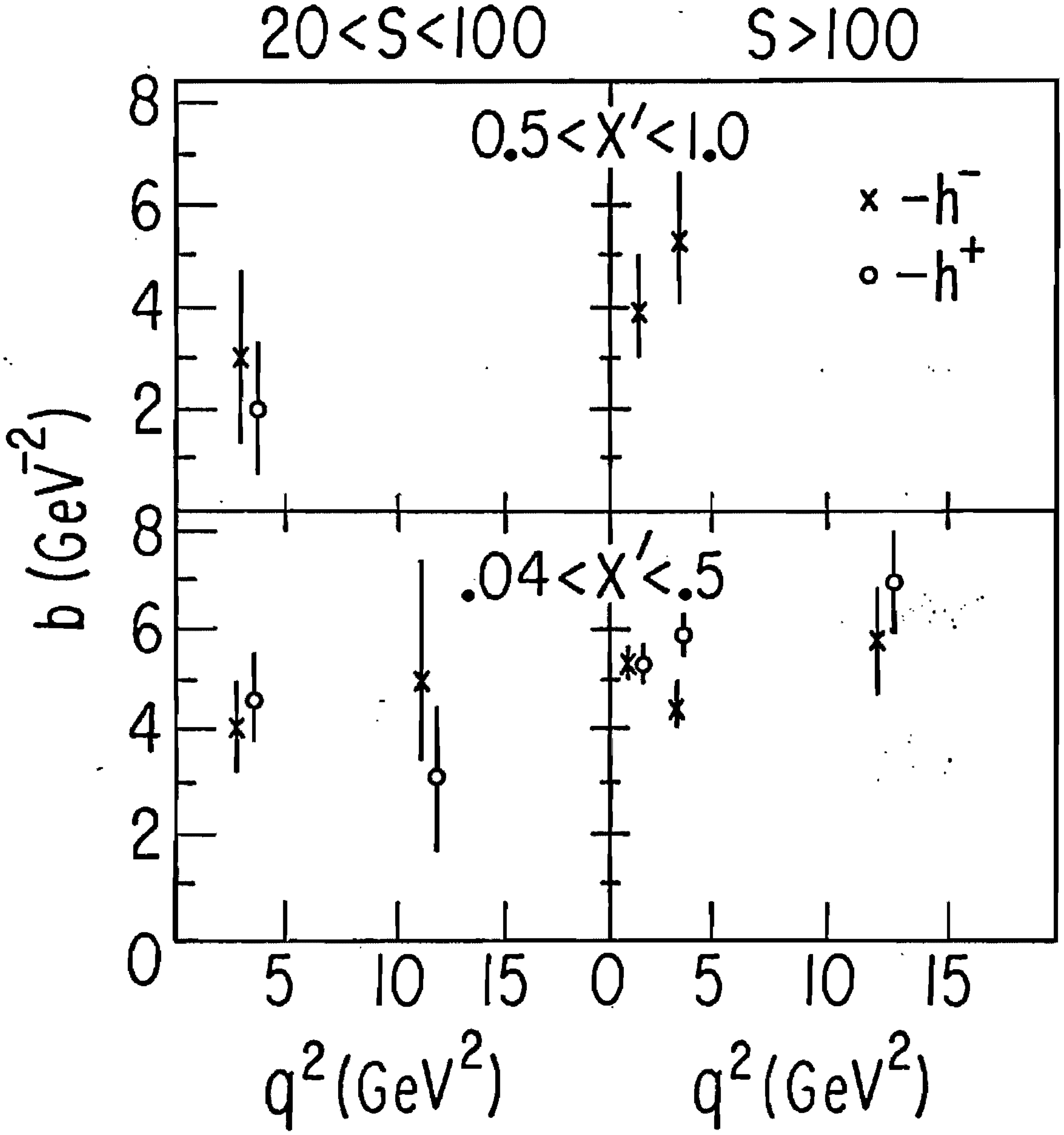
20<S<100
S>100
0.5<X′<1.0
.04<X′<.5
× –h⁻
○ –h⁺
b (GeV⁻²)
8
6
4
2
0
5
10
15
q²(GeV²)
q²(GeV²)

Figure 19. $G(P_T^2)$ fit to $\exp(-bP_T)$. The q^2 intervals are the same as those used in Figure 12.

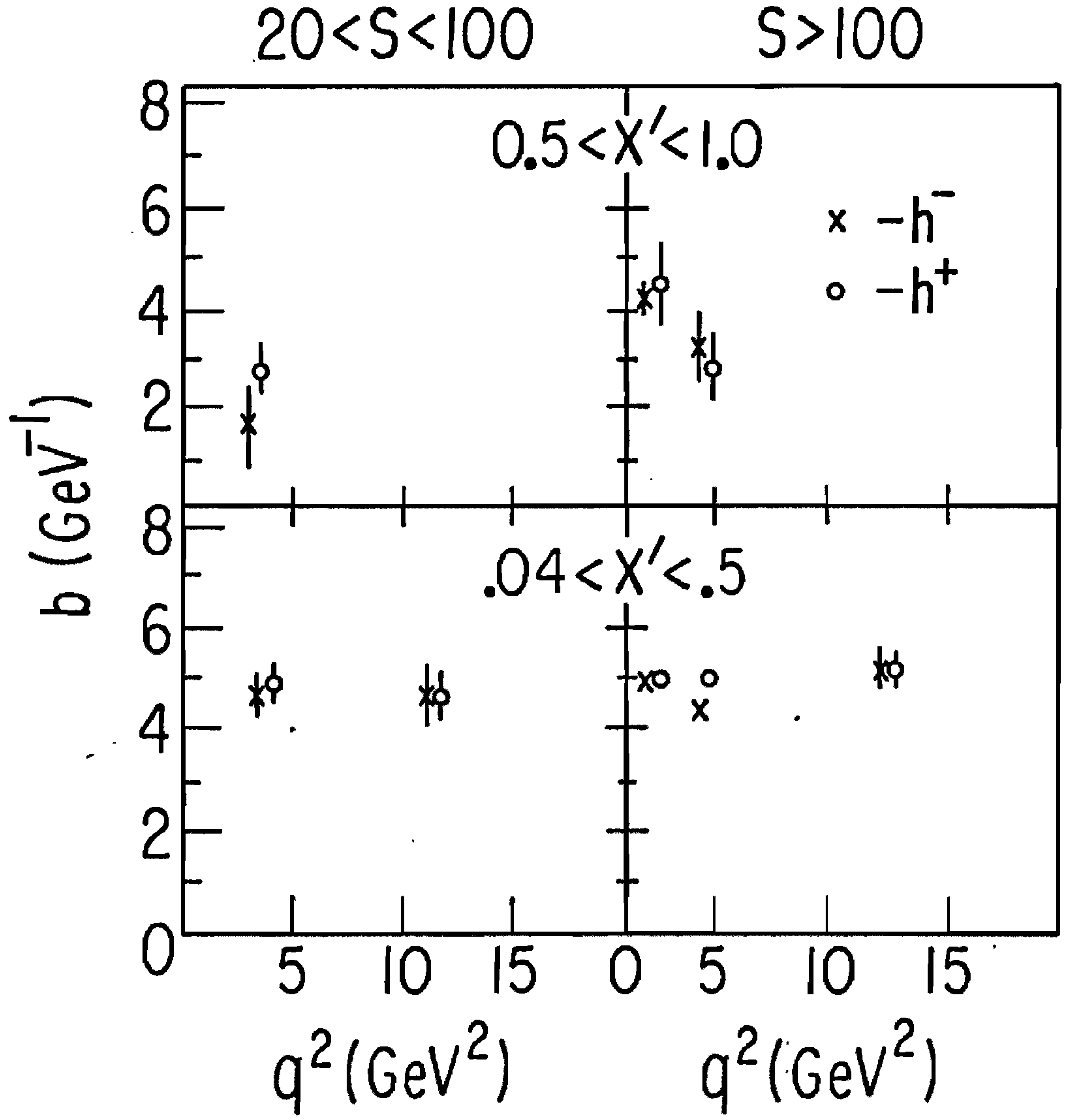
20<S<100
S>100
0.5<X'<1.0
.04<X'<.5
x -h⁻
o -h⁺
b (GeV⁻¹)
8
6
4
2
0
5
10
15
0
5
10
15
q²(GeV²)
q²(GeV²)

Figure 20. Transverse momentum spectrum for charged hadrons. A is in the range $0.04 < x' < 0.5$; B is $0.5 < x' < 1.0$. The fits (see Table 3) of the form $\exp[-b(P_T^2 + M^2)^{1/2}]$ are for the negative hadrons.

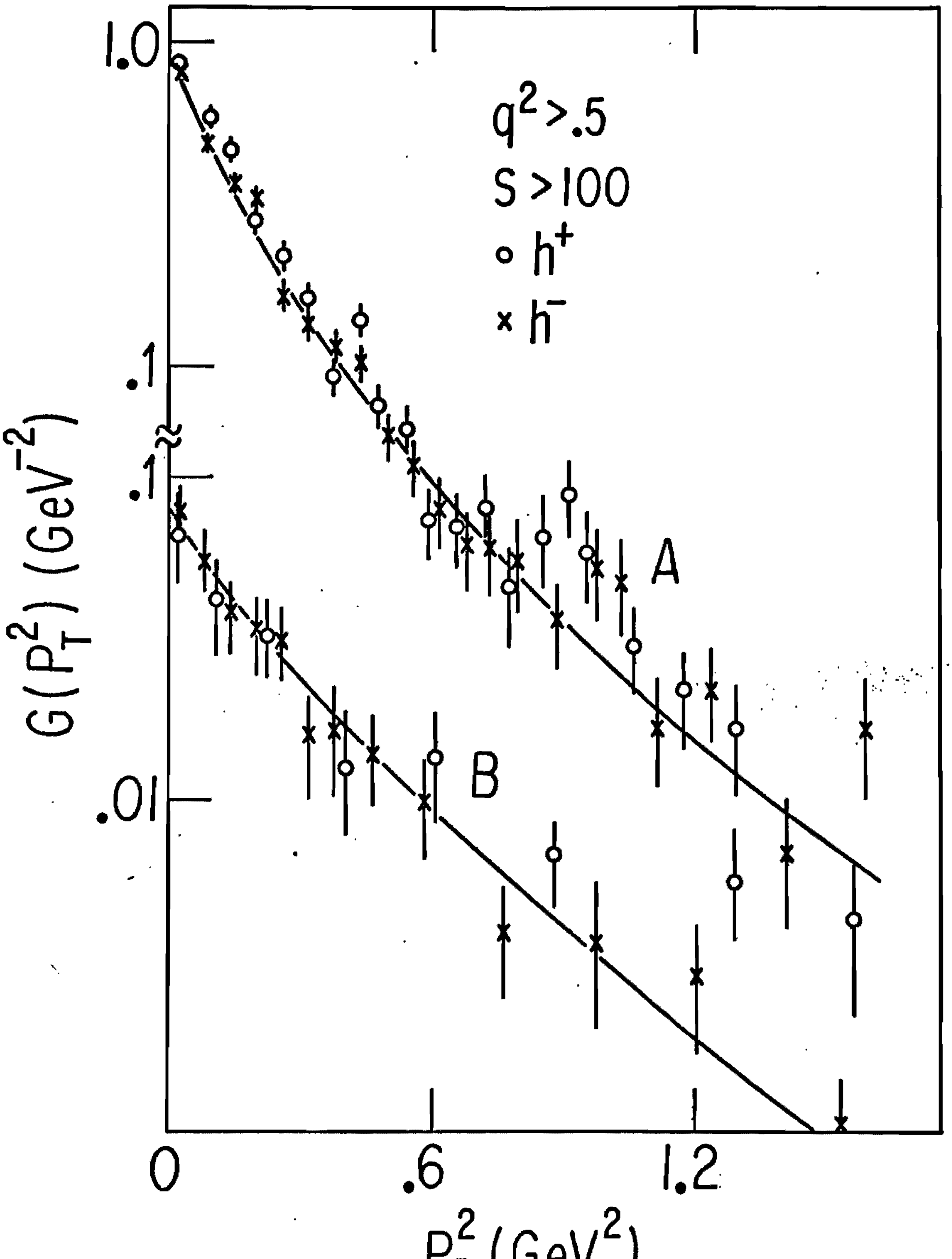
1.0
.1
.1
.01
G(P_T^2) (GeV^-2)
q^2 > .5
S > 100
○ h^+
× h^-
A
B
0
.6
1.2
P_T^2 (GeV^2)

Figure 21. The b and M estimates for the $\exp[-b(P_T^2 + M^2)^{1/2}]$ fits to the transverse momentum distributions of inclusive hadrons. Lo x' means $0.04 < x' < 0.5$; Hi x' means $0.5 < x' < 1.0$; Lo s means $20 < s < 100$ GeV^2; Hi s means $s > 100$ GeV^2.

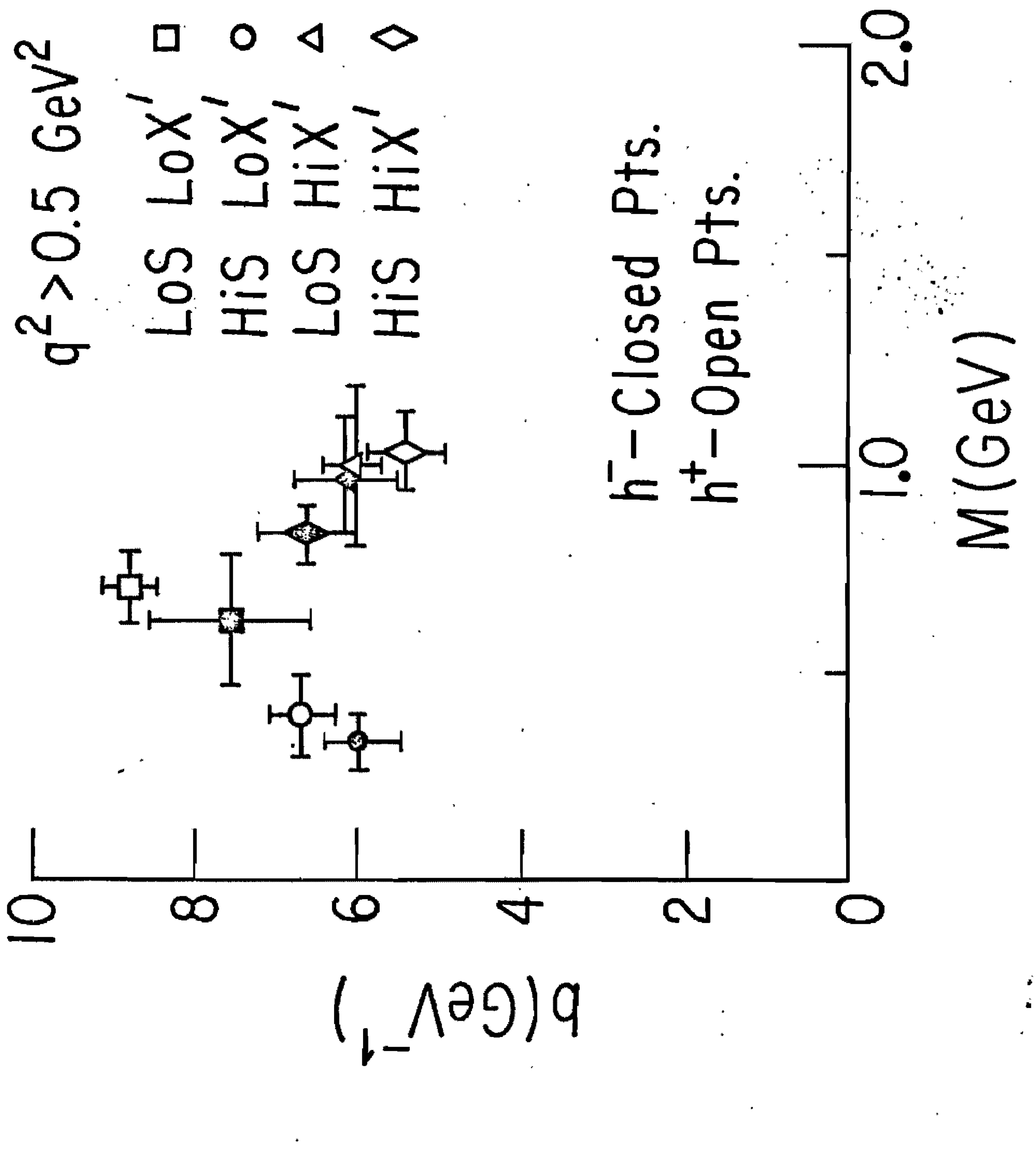
$q^2 > 0.5$ GeV^2
LoS LoX′ □
HiS LoX′ ○
LoS HiX′ △
HiS HiX′ ◇
h^- – Closed Pts.
h^+ – Open Pts.
b(GeV^{-1})
10
8
6
4
2
0
1.0
2.0
M (GeV)

Figure 22. $\langle P_T \rangle$ plotted as function of x' for two s regions.

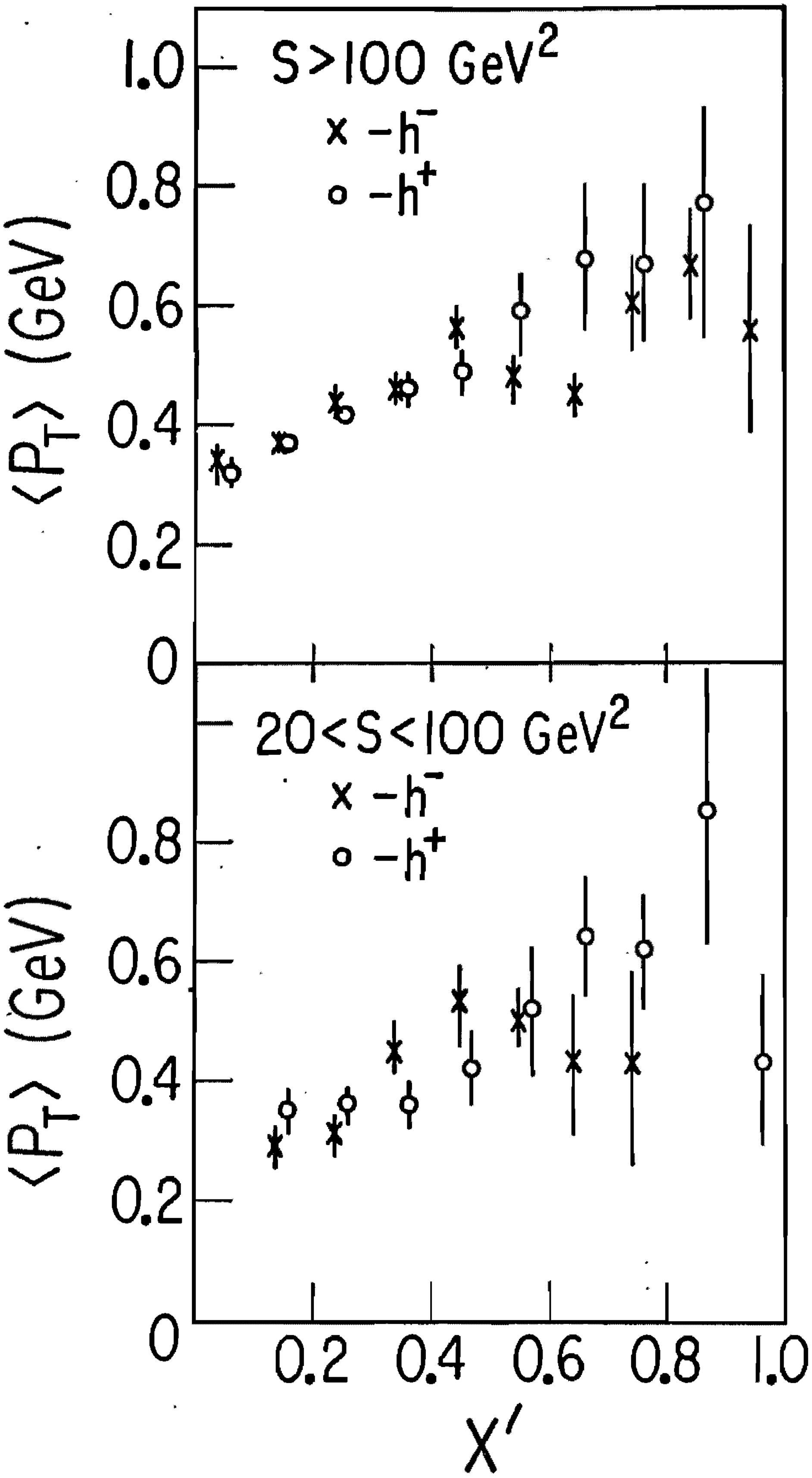
S>100 GeV^2
x -h$^-$
o -h$^+$
20<S<100 GeV^2
x -h$^-$
o -h$^+$
⟨P$_T$⟩ (GeV)
⟨P$_T$⟩ (GeV)
1.0
0.8
0.6
0.4
0.2
0
0.8
0.6
0.4
0.2
0
0.2
0.4
0.6
0.8
1.0
X′